Numerical study of spray combustion of a biodiesel surrogate fuel using the LES-FGM approach

Constantin Sula[a], Holger Grosshans[b], Miltiadis V. Papalexandris[a,*]

[a]*Institute of Mechanics, Materials and Civil Engineering, Université catholique de Louvain, Place du Levant 2, Louvain-la-Neuve, 1348, Belgium.*
[b]*Physikalisch-Technische Bundesanstalt (PTB), Bundesallee 100, Braunschweig, 38116, Germany.*

Abstract

In this paper, we report on Large Eddy Simulations (LES) of spray combustion of a Karanja Methyl Ester (KME) biodiesel surrogate. The surrogate fuel considered herein is a blend of n-dodecane and methyl butanoate. In terms of combustion modelling, we employ a specific implementation of the Flamelet Generated Manifold (FGM) approach, according to which the energy equation is cast in terms of the sensible enthalpy. This approach allows for the direct computation of the temperature and the temperature-dependent properties of the mixture, which results in significant computational savings. Concerning the numerical methodology, we employ the Eulerian approach for the gaseous phase, coupled with Lagrangian particle tracking for the motion of the fuel droplets. Our numerical setup follows closely the well-known "Spray A" operating conditions. Three different cases are considered herein: in the first two cases we employ the thermophysical properties of the liquid surrogate fuel and two different values of the oxygen concentration (15% and 21% respectively). In the third case, the so-called "hybrid" one, we employ the properties of the liquid KME itself; these are considerably different than those of the liquid surrogate fuel. Therefore the hybrid case is in principle more representative of the spray combustion of the actual KME. According to our numerical results, the ignition of

*Corresponding author
Email address: miltos@uclouvain.be (Miltiadis V. Papalexandris)

the surrogate fuel consists of the same stages as those observed in n-dodecane flames. In the first case (15% O_2), the flame topology remains the same as in the combustion of (pure) n-dodecane. The Ignition Delay Time (IDT) and combustion temperature also remains practically unchanged while the Flame Lift-off Length (FLOL) increases by 12%. When the O_2 concentration increases from 15% and 21%, the IDT increases by approximately 17% and the combustion temperature by approximately 11%, while the FLOL decreases by roughly 9%. On the other hand, the liquid fuel properties have a significant impact on the combustion process and flame topology. In particular, in the combustion of KME there is an increased number of ignition kernels on the periphery of the jet and a large decrease of the FLOL, by approximately 50%. Moreover, our simulations predict that with KME there is production of acetylene in low-temperature zones, which can impact the levels of soot formation.

Keywords: Large Eddy Simulation, biodiesel, combustion modelling, alternative fuels, Karanja Methyl Ester, Flamelet Generated Manifolds

1. Introduction

The use of alternative renewable fuels for engine applications has attracted much attention due to increased concerns over the use of fossil fuels and stringent environmental regulations. Biodiesel can be a viable alternative to fossil fuels for power generation and propulsion of transportation systems with promising results regarding soot formation [1, 2]. Nonetheless, NO emissions remain a major concern for the broader use of biodiesel fuels.

In the recent past, various experimental and numerical studies have been carried out to assess the impact of the physical properties of biofuels on the evolution of the spray. For example, Bohl et al. [3] investigated the macroscopic characteristics of biofuel sprays in constant-volume spray vessels and reported that the fuel viscosity considerably influences the spray cone angle and the fuel-oxidizer mixture process. Also, Corral-Gomez et al. [4] studied the impact of various fuel properties on the characteristics of sprays by utilising ternary blends

of diesel-biodiesel-ethanol and concluded that the fuel density affects spray tip penetration. In contrast, the spray cone angle was affected mainly by the fuel kinematic viscosity and surface tension. Similarly, Han et al. [5] studied the properties of sprays of methyl esters, which constitute important components of biodiesel, under different injection and ambient pressures.

Knowledge of both liquid and vapour fuel properties is necessary in order to perform reliable spray and combustion modelling of the fuel in hand. However, experimental measurements of biodiesel properties over a broad range of temperatures is cost-intensive, laborious and time-consuming. This difficulty can, in principle, be circumvented by considering a surrogate fuel or by using existing correlations to estimate the thermophysical properties of the fuel of interest on the basis of its composition. For example, suitable correlations for blends containing methyl esters are available in [6–9]. Additionally, by using a surrogate, one can employ a compact reaction mechanism to replicate the combustion properties of the biodiesel, which helps keeping the computational cost of simulations at reasonable levels. However, surrogate fuels are typically formulated so as to approximate the chemical kinetics of the combustion of the actual fuel. Whereas the properties of the liquid surrogate can be substantially different from those of the liquid fuel itself. This, in turn, can impact the spray properties, as well as the fuel evaporation and mixing prior to ignition.

With respect to spray modelling, many numerical studies have been carried out for both non-reacting and reacting fuel sprays. Typically, under engine-relevant conditions, the fuel jet has a very short liquid core which results into rapid atomisation and evaporation [10]. For this reason, a popular approach is not to directly solve for the atomisation process but to account for it by sampling the initial droplet diameters via a prescribed probability distribution function [11–15]. On the other hand, the breakup of the fuel droplets is directly solved for by incorporating an appropriate breakup model.

In spray combustion it is quite common to combine Lagrangian Particle Tracking for the spray with the Large Eddy Simulation (LES) approach for the gaseous mixture. According to previous studies [16–21], this methodology can

accurately capture the main characteristics of the spray jet, e.g., liquid length, vapour penetration distance and mixture formation. Further, performing a fuel spray simulation requires a combustion model with the capacity to accommodate complex chemical kinetic while taking into account turbulence-chemistry interactions in a reliable manner. Biodiesel fuels typically comprise alkyl fatty acid (chain length $C_{14} - C_{22}$) and esters of short-chain alcohols, primarily methanol or ethanol [22]. These components are present in different concentrations, depending on the source of the specific biodiesel. Detailed kinetic mechanisms developed for these components run into several thousands of species and reactions [23]. To circumvent the difficulty in utilising such large kinetic schemes, one may employ kinetic schemes of surrogate fuels which are typically less complex. Recent studies [17, 24–26] have shown that this approach is reliable, cost effective and can be efficiently used in spray combustion simulations. Based on our previous numerical study of n-dodecane spray flames [27], we may infer that the Flamelet Generated Manifolds combustion model in conjunction with LES is a robust technique that can accurately capture the main characteristics of spray combustion.

This paper is concerned with the numerical simulations of spray combustion of Karanja oil Methyl Ester (KME). To the best of our knowledge, such simulations are currently unavailable in the literature. In our study we address several issues of biodiesel spray flames that currently remain open. First, we compare the combustion process of the biodiesel surrogate with that of the corresponding diesel surrogate, i.e. the n-dodecane. Further, we analyse the impact of the liquid-fuel properties on the spray evolution and ignition. Additionally, we investigate the influence of the initial oxygen concentration on the combustion of the biodiesel surrogate. The overarching objective of the present study is to provide information that will help assess whether current diesel engines can efficiently operate with biodiesel fuel without significant modifications.

In our simulations, we employ a blend of n-dodecane and methyl butanoate as a KME surrogate, along with the chemical kinetics mechanism developed in [28] for this blend. Additionally, in relation to the aforementioned second ob-

jective, we perform simulations with different setups: one using the liquid-fuel properties of the surrogate and another one using those of KME. The latter approach (combustion model of the surrogate combined with the liquid properties of the fuel) is the so-called "hybrid strategy" put forward by Anand et al. [29] in order to take into account the substantial differences between the properties of the two liquid fuels.

Although the essential thermophysical properties for KME biofuels such as density, viscosity, vapour pressure, and heat capacity have been made available to us [30], there is a marked scarcity of data for other important properties, namely, latent heat evaporation, flash point and thermal conductivity. These are approximated using suitable correlations based on the methyl ester content of KME [7].

The paper is structured as follows. In Section 2 we outline the mathematical model and the algorithm for its numerical treatment. In Section 3 we briefly present the reaction mechanism of the biodiesel surrogate and elaborate on the method of calculation of the unknown properties of liquid KME. In Section 4 we describe the computational setup, including initial conditions and meshing. Section 5 contains a detailed presentation and discussion of the numerical results. Finally, Section 6 concludes.

2. Mathematical and Numerical modelling

The LES of our study are based on the spatially-filtered, compressible Navier-Stokes-Fourier equations. To this end, we employ the density-weighted operator of Favre [31]. More specifically, for a generic quantity ψ, the corresponding Favre-filtered quantity $\widetilde{\psi}$ is defined as $\widetilde{\psi} = \overline{\rho\psi}/\overline{\rho}$, where $\overline{\rho}$ and $\overline{\rho\psi}$ are spatially-

filtered quantities. Using standard notation, the filtered mass, momentum and energy balance laws of the gaseous phase read, [15, 17],

$$\frac{\partial \overline{\rho}}{\partial t} + \nabla\cdot\left(\overline{\rho}\widetilde{\boldsymbol{u}}\right) = \overline{\Gamma}\,, \tag{1}$$

$$\frac{\partial\left(\overline{\rho}\widetilde{\boldsymbol{u}}\right)}{\partial t} + \nabla\cdot\left(\overline{\rho}\widetilde{\boldsymbol{u}}\widetilde{\boldsymbol{u}}\right) = -\nabla\overline{p} + \nabla\cdot\left(\left(\overline{\mu}+\mu_{\mathrm{t}}\right)\widetilde{\boldsymbol{V}}^{\mathrm{d}}\right) + \overline{\boldsymbol{F}}\,, \tag{2}$$

$$\begin{aligned}\frac{\partial\left(\overline{\rho}\widetilde{h}_{\mathrm{s}}\right)}{\partial t} + \nabla\cdot\left(\overline{\rho}\widetilde{h}_{\mathrm{s}}\widetilde{\boldsymbol{u}}\right) &= -\frac{1}{2}\frac{\partial\left(\overline{\rho}\left|\widetilde{\boldsymbol{u}}\right|^2\right)}{\partial t} - \frac{1}{2}\nabla\cdot\left(\overline{\rho}\left|\widetilde{\boldsymbol{u}}\right|^2\widetilde{\boldsymbol{u}}\right) + \frac{\partial\overline{p}}{\partial t}\\ &+\nabla\cdot\left(\left(\overline{\mu}+\mu_{\mathrm{t}}\right)\widetilde{\boldsymbol{V}}^{\mathrm{d}}\cdot\widetilde{\boldsymbol{u}}\right) + \nabla\cdot\left(\left(\frac{\overline{\kappa}}{\overline{c}_p}+\frac{\kappa_{\mathrm{t}}}{\overline{c}_p}\right)\nabla\widetilde{h}_{\mathrm{s}}\right) + \overline{S}_{\mathrm{h}} + \overline{Q}\,,\end{aligned} \tag{3}$$

where $\widetilde{h}_{\mathrm{s}}$ stands for the filtered sensible enthalpy and $\widetilde{\boldsymbol{V}}^{\mathrm{d}}$ for twice the deviatoric part of the filtered strain-rate tensor, $\widetilde{\boldsymbol{V}}^{\mathrm{d}} = \left(\nabla\widetilde{\boldsymbol{u}} + \left(\nabla\widetilde{\boldsymbol{u}}\right)^{\top}\right) - \frac{2}{3}\nabla\cdot\left(\overline{\rho}\widetilde{\boldsymbol{u}}\right)\boldsymbol{I}$.

The source terms $\overline{\Gamma}$, $\overline{\boldsymbol{F}}$ and $\overline{S}_{\mathrm{h}}$ in (1)–(3) represent, respectively, exchange of mass, momentum and energy between the continuous gaseous phase and the fuel droplets. Their explicit form is provided in [15] and is not included herein for the purposes of economy of space. The second source term in the energy equation (3), $\overline{Q}$, accounts for the heat release due to combustion. It is equal to the sum, over all gaseous species, of the formation enthalpy of each species multiplied by its reaction rate [32, 33].

In the context of tabulated chemistry, the above governing system is supplemented with transport equations for the filtered mixture fraction $\widetilde{Z}$ and progress variable $\widetilde{\mathcal{Y}}$ and with an algebraic relation for the mixture-fraction variance. In our study, the mixture fraction Z is given as the coupling function ζ normalized by Bilger's weight factors ζ_0 and ζ_1 [34, 35]; in other words,

$$Z = \frac{\zeta-\zeta_0}{\zeta_1-\zeta_0}\,, \tag{4}$$

with

$$\zeta = 2\frac{Y_{\mathrm{C}}}{W_{\mathrm{C}}} + \frac{1}{2}\frac{Y_{\mathrm{H}}}{W_{\mathrm{H}}} - \frac{Y_{\mathrm{O}}}{W_{\mathrm{O}}}\,, \tag{5}$$

where W_i denotes the atomic mass of element i. The weight factors ζ_0 and ζ_1 are constants evaluated in the fuel and oxidizer streams, respectively, of the

corresponding 1D counter-diffusion (CD) flame. Also, herein $\mathcal{Y}$ is given as a linear combination of three reaction products, CH_2O, CO and CO_2, namely,

$$\mathcal{Y} \;=\; \frac{Y_{\mathrm{CO_2}}}{M_{\mathrm{CO_2}}} + \frac{Y_{\mathrm{CO}}}{M_{\mathrm{CO}}} + \frac{Y_{\mathrm{CH_2O}}}{M_{\mathrm{CH_2O}}}\,, \tag{6}$$

where M_i is the molar mass of the species i non-dimensionalized by the molar mass of atomic hydrogen. In general, $\mathcal{Y}$ can be defined as a convex linear combination of any chemical species, provided that it is increasing monotonically from the initial mixing solution to chemical equilibrium and that it accounts for all combustion stages. The above definition was employed in previous studies with n-dodecane [17, 19, 27, 36] which is the main component of the biodiesel surrogate, and is therefore retained herein. Nonetheless, other choices may improve the accuracy of the computations, depending on the fuel, chemical kinetics mechanism and ambient conditions; see, for example, the comparative study in the recent article [37].

The filtered transport equations for $\widetilde{Z}$ and $\widetilde{\mathcal{Y}}$ read,

$$\frac{\partial \overline{\rho}\widetilde{Z}}{\partial t} + \nabla\cdot\left(\overline{\rho}\widetilde{\boldsymbol{u}}\widetilde{Z}\right) \;= \nabla\cdot\left(\overline{\rho}\widetilde{\boldsymbol{u}}\widetilde{Z} - \overline{\rho}\widetilde{\boldsymbol{u}Z}\right) + \nabla\cdot\left(\overline{\rho}\overline{D}\nabla\widetilde{Z}\right) + \overline{\Gamma}\,, \tag{7}$$

$$\frac{\partial \overline{\rho}\widetilde{\mathcal{Y}}}{\partial t} + \nabla\cdot\left(\overline{\rho}\widetilde{\boldsymbol{u}}\widetilde{\mathcal{Y}}\right) \;= \nabla\cdot\left(\overline{\rho}\widetilde{\boldsymbol{u}}\widetilde{\mathcal{Y}} - \overline{\rho}\widetilde{\boldsymbol{u}\mathcal{Y}}\right) + \nabla\cdot\left(\overline{\rho}\overline{D}\nabla\widetilde{\mathcal{Y}}\right) + \overline{\dot{\omega}}_{\mathcal{Y}}\,. \tag{8}$$

For the subgrid variance of the mixture fraction we use the algebraic model [38],

$$\widetilde{Z''^2} \;=\; \widetilde{Z^2} - \widetilde{Z}^2 \;=\; C_{\mathrm{v},Z}\,\Delta^2\left|\frac{\partial\widetilde{Z}}{\partial x_j}\right|^2\,. \tag{9}$$

where $C_{\mathrm{v},Z}$ represents the model constant which is dynamically evaluated according to the process described [39] and Δ denotes the LES filter width.

The resulting governing system is closed with the ideal gas law. The viscosity and thermal diffusivity of the gaseous phases are computed according to the relations provided in [40], on the basis of the six dominant species of the reactive gas (reactants and final products). The transport and thermophysical properties for any given gaseous species, are evaluated via the intermolecular potential model for rigid spheres and 7th-order polynomial interpolation [41].

With regard to the subgrid-scale modelling, the eddy viscosity, μ_{t}, is computed via the dynamic k-equation model [42, 43]. The thermal diffusivity, κ_{t}, is computed from μ_{t} by assuming that the turbulent Prandtl number is constant and equal to unity. The unresolved turbulent fluxes in (7) and (8) are also modeled via a gradient assumption by setting the turbulent Schmidt number equal to unity.

In the context of LES, the various filtered quantities are expressed in terms of Z and $\mathcal{Y}$ via a presumed joint Probability Distribution Function (PDF). However, the range of $\mathcal{Y}$ depends on Z, which in turn implies that $\mathcal{Y}$ and Z are not statistically independent. For this reason, one typically introduces the scaled progress variable $\mathcal{C}$,

$$\mathcal{C} \;=\; \frac{\mathcal{Y} - \mathcal{Y}_{\min}\left(Z\right)}{\mathcal{Y}_{\max}\left(Z\right) - \mathcal{Y}_{\min}\left(Z\right)}\,. \tag{10}$$

As per [44], $\mathcal{C}$ and Z are only weakly dependent. Accordingly, in the present study we assume that Z and $\mathcal{C}$ can be treated as statistically independent. Further, we consider that they follow the beta and delta-function distributions, respectively. Therefore, a generic filtered quantity $\widetilde{\psi}$ is expressed as,

$$\widetilde{\psi} \;=\; \int\int \psi(Z,\mathcal{C})\,\beta(Z;\widetilde{Z},\widetilde{Z''^2})\;\delta(\widetilde{\mathcal{C}}-\mathcal{C})\,dZ\,d\mathcal{Y}\,. \tag{11}$$

Strictly speaking, the approximation of the distribution of $\mathcal{C}$ by a delta function is valid for infinitely fast chemistry. Nonetheless, for the purposes of our study, we may assume that the chemical reactions are still fast enough so that the error of this approximation is acceptable.

The source terms $\overline{Q}$ and $\overline{\dot{\omega}}_{\mathcal{Y}}$ of (3) and (8) and the mass fractions of species of interest are computed as function of $\widetilde{Z}$, $\widetilde{\mathcal{C}}$ and $\widetilde{Z''^2}$ via a lookup procedure from the FGM database. Also, unity Lewis number is assumed. This is a common assumption in numerical simulations of turbulent combustion of diesel surrogates; nonetheless, in the flamelet regime, non-unity Lewis-number effects may be non-negligible. The flamelet equations for the CD flames are integrated numerically via the flame solver *Ember* [45] and the thermophysical properties entering these equations are computed with the software *Cantera* [46]. For

more details regarding the flamelet solutions and the construction of the FGM database, the reader is referred to [27].

In the current implementation of the FGM-LES methodology, the density and thermophysical properties of the gaseous mixture are calculated on the basis of six major species: $C_5H_{10}O_2$, $C_{12}H_{26}$, O_2, CO_2, H_2O and N_2, i.e. the reactants and final products. Inside the reaction zones, the sum of the concentrations of these six species is not unity. For this reason, the mass fraction of N_2 is calculated on the basis of the mass fractions of the other five species, thus enforcing that the sum of the mass fractions of the corresponding species is equal to unity. According to our previous study [27] of spray with n-dodecane, the error induced by this simplification is quite small and for this reason it is retained herein.

The governing equations (1)–(3) are solved numerically via a finite-volume algorithm. According to it, integration in time is performed via the implicit Euler scheme, while the convective and diffusive terms are discretized via the 2nd-order upwind scheme and 2nd-order centered differences, respectively. The computation of the pressure and velocity fields is performed with the compressible version of the Pressure Implicit Splitting of Operators (PISO) technique [47], according to which the continuity equation acts as a constraint to the pressure field.

The discrete liquid phase is solved for via the Lagrangian particle tracking approach, combined with the stochastic parcel method [48]. In this method, the fuel droplets are grouped into parcels and then each parcel is treated as a Lagrangian point and tracked individually. The momentum and energy equations of the droplets, as well as a detailed description of the related submodels, are described in detail in [15]. These equations are endowed with well-known correlations for evaporation and heat transfer at the droplet surface [49–51]. Also, since the primary breakup occurs very close to the nozzle exit, it is not directly solved for. Nonetheless, it is taken into account by using the Rosin-Rammler distribution for the initial droplet diameter. The breakup of the droplets is modeled using the modified version (MTAB) [15] of the popular Taylor analogy

breakup model [52]. The model sensitivity with respect to droplet breakup and mesh size for non-reacting and reacting flows with n-dodecane has been assessed in [15] and [27], respectively.

3. Reaction mechanism and thermophysical properties

As mentioned in the Introduction, the reaction mechanisms of biodiesel fuels are too complex to be directly applied in numerical simulations. So it is convenient to introduce a surrogate fuel, for which a simpler reaction mechanism can be developed. The principal idea behind this strategy is to identify a less complex mixture that emulates to a sufficient level of accuracy the essential performance characteristics of the actual biodiesel, such as carbon content, heating value, cetane number etc. In the current study, following the analysis of [28], the molar composition of the surrogate fuel is 35.68 % methyl butanoate ($C_5H_{10}O_2$) and 64.32 % n-dodecane ($C_{12}H_{26}$). This composition is derived by directly matching the molecular structure and key functional groups of the Karanja Methyl Ester (KME) [53]. The surrogate fuel was conceived in [28] so as to retain the main characteristics, main functional groups, and the H/C and O/C ratios of the KME biodiesel.

Regarding chemical kinetics, the authors of [28] combined two well-validated reaction mechanisms for n-dodecane (255 species, 1524 reactions) [54] and methyl butanoate (275 species, 1545 reactions) [55]. In particular, they initially derived a compact mechanism for methyl butanoate from the detailed reference mechanism, using the Directed Relation Graph with Error Propagation (DRGEP) [56] reduction technique. According to this technique, the influence of an error introduced by the change of the concentration of a species, or by discarding the species entirely from the initial mechanism, is damped as it propagates along the graph to reach the targets. The targets are some desirable chemical features that the reduced mechanism is expected to reproduce over a predefined range of physical conditions. They can be as diverse as ignition properties, burning velocities and levels of soot precursors. By employing the DRGEP technique,

the initial mechanism is reduced to a simpler one that consists of 255 species and 1132 reactions. Additionally, a sub-model describing methanol kinetics is incorporated within the skeletal model, resulting to a system consisting of 275 species and 1545 reactions

Subsequently, the reaction mechanism [54] for n-dodecane, is augmented with the oxidation pathways of methyl butanoate. The resulting combined mechanism for the surrogate fuel consists of 275 species and 2431 reactions [28]. According to its authors, this mechanism matches the corresponding detailed-model computations for these components within 5% error. For a detailed description of the reduction procedure, the reader is referred to the original publications [28, 56].

Reliable spray combustion modelling and simulation, requires knowledge of the transport and thermophysical properties of both liquid fuel and its vapour. As mentioned in the introduction, for the hybrid case, the properties of the liquid fuel are represented by the actual KME biodiesel, while the properties of the vaporized fuel are taken to be those of its surrogate. Since the species that comprise the surrogate, n-dodecane and methyl butanoate, are well studied, their properties (for both liquid and gaseous phases) are readily available in the literature.

On the other hand, there is a marked scarcity of data regarding the properties of the liquid KME. Below we present the methodology employed to evaluate the unknown properties of KME for the purposes of our study. Certain properties like density, vapour pressure, viscosity and calorific value for the liquid KME biodiesel, have been experimentally measured and provided by Moshammer [30]. These properties have been tabulated as a function of temperature using third-order polynomial fits and are used for the "hybrid" case. The surface tension of KME is approximated by that of canola oil [57]. KME biodiesel is synthesized from non-edible Karanja oil through a transesterification process [58]. The fatty acid methyl ester composition of the KME biodiesel [59] is provided in the Table 1, and is mainly composed of oleic acid (C18:1) and linoleic acid (C18:2).

Table 1: Composition (% by mass) of KME [59]

Palmitic acid (C16:0)	8.6
Octadecanoic acid (C18:0)	7.8
Oleic acid (C18:1)	53.8
Linoleic acid (C18:2)	17.6
Linolenic acid (C18:3)	4.1
Arachidic acid (C20:0)	1.2
Behenic acid (C22:0)	5.1
Tetracosanoic acid (C24:0)	1.4

To calculate the remaining unknown properties of the KME biodiesel, namely, boiling point, critical pressure, critical temperature and critical volume, we first evaluate the corresponding properties of each component of KME, as provided in Table 1 from available correlations and then apply the appropriate mixing rule for each unknown property. Most of these correlations are provided in terms of the composition and chemical structure of the component. The correlations used herein were selected on the basis of their applicability in the chemical structure of a given component and accuracy. These correlations require knowledge of additional quantities such as acentric factor, molar mass, group contribution parameters in methyl esters' molecular structure, and reduced properties (pressure, volume and temperature). A wealth of correlations and instructions on how to use them for a specific component of Table 1 can be found in [6]. Additionally, Anand et al. [7] carried out an analysis of the predictive capacity of various available correlations for methyl esters. Following the findings in [7], we provide below the selected correlations for our study.

The normal boiling point, $T_{\mathrm{nb}i}$, of the i-th component of the mixture is evaluated according to the relation proposed by Constantinou-Gani [60], which is based on the group contribution method [61]. For the critical temperature T_{ci}, pressure P_{ci} and molar volume $V_{\mathrm{c}i}$ of the i-th component we employ the

relations proposed by Joback [62]. Then, the critical temperature T_{cm} and molar volume $V_{\mathrm{cm}i}$, of the mixture are calculated as the mole-fraction averages; this process is often referred to as *Kay's rule* [63]. While the critical pressure of the mixture, P_{cm} is calculated according to the rule provided in [64].

Further, for the latent heat of evaporation, heat capacity and thermal conductivity of the mixture, we first compute the corresponding property of each component from the correlations in [41]. These are provided in the form of 7th-order polynomial fits of experimental data. Then, the mixture properties are computed as the mole-fraction averages of the corresponding properties of its components. As pointed out in [6], this approach is not always accurate, especially for a mixture of many components. However, according to the composition mentioned in Table 1, the biodiesel considered herein consists primarily of two components, oleic and linoleic acids. Therefore, the error in the computation of these properties is expected to be small.

Finally, it is noted that, in the case of fuel blends, the various components evaporate at different rates due to different thermophysical properties (such as diffusivity, vapour pressure etc). This is the phenomenon of differential evaporation. In principle, one can evaluate the evaporation rate of each fuel component separately. However, in this case, the vaporized unreacted fuel does not have a uniform composition inside the combustion chamber. This, in turn, necessitates the construction of a whole series of FGM databases with different ratios of components that can be used for interpolating the result to the specific ratio at any given point during the simulation of the combustion of the spray. This approach however, is quite cumbersome to implement and, from the computational point of view, prohibitively expensive. For this reason, in this work we assume that the vaporized fuel has the same ratio of components as the liquid fuel, while the relevant thermophysical properties of the liquid fuel are computed as mole-fraction averages of its components. Since in the cases "15%O_2" and "21%O_2" the liquid fuel consists of two components and in the hybrid case the biodiesel consists primarily of two components, we expect that the error of not accounting for differential evaporation to be relatively small.

4. Computational set-up

As mentioned above, the initial conditions for the investigated cases follow closely the set up of the reactive "Spray A" configuration. According to it, the initial pressure, temperature and density of the surrounding gas (oxidizer) are 6 MPa, 900 K and 22.8 kg/m^3, respectively. The liquid fuel is injected under the pressure of 150 MPa through a nozzle of a 90 μm diameter under a prescribed flow rate which corresponds to a total mass of 3.5 mg of injected fuel. The initial temperature of the incoming liquid-fuel jet is 363 K. The direction of injection of the parcels is chosen randomly within the prescribed spray cone, while the initial droplet diameter of the parcels is assumed to follow the Rosin-Rammler distribution. For all cases, the amount of injected parcels throughout a single simulation is set to 1.2×10^6.

Table 2: Fuel properties and ambient molar gas compositions for each of the three cases considered herein.

Case name	"15% O_2"	"21% O_2"	"15% O_2 hybrid"
Fuel	surrogate	surrogate	KME
Density [kg/m^3] @ 293 K	781.17	781.17	887.95
Viscosity [mPa*s] @ 293 K	1.09	1.09	7.61
Surface tension [mN/m] @ 293 K	25.20	25.20	31.14
O_2(%)	15	21	15
N_2 (%)	75.15	69.33	75.15
CO_2 (%)	6.23	6.11	6.23
H_2O (%)	3.62	3.56	3.62

In relation to the objectives of our study, we define three distinct cases, in terms of the initial oxygen concentration of the ambient gas (the oxidizer) and the thermophysical properties of the liquid fuel. In order to assess the impact of the initial oxygen concentration, two different cases are considered namely,

15% and 21%. Their respective molar gas compositions are provided in Table 2. These compositions are chosen so as to resemble those in actual diesel engines after several cycles and account for exhaust gas recirculation. These two cases, are referred to herein as "15% O_2" and "21% O_2" respectively. In both of these cases, the properties of the liquid fuel and fuel vapour are taken to be those of the surrogate fuel.

For the third case, we employ the hybrid approach proposed by Anand et al. [29]. According to it, the thermophysical properties of the liquid fuel are those of the actual biodiesel. Whereas the properties of the fuel vapour are those of the surrogate blend. This strategy is deemed more appropriate for numerical simulations because the surrogate fuel has been conceived so as to match the combustion characteristics of the actual fuel; therefore, the thermophysical properties of the droplets of the surrogate differ considerably from those of the actual fuel. On the other hand, in the absence of data for the properties of the biodiesel vapour, we necessarily use those of the surrogate fuel vapour. The initial oxygen molar concentration of the ambient gas for this case is set to 15% O_2. For this reason, the hybrid case will be referred to as "15% O_2 hybrid" case.

For all three cases, the computational mesh is identical to that of our previous study of spray combustion of n-dodecane [27]. More specifically, the computational domain is a cuboid with rigid and adiabatically isolated walls. Its length is 80 mm and its cross-section measures 20 mm $\times$ 20 mm. For the discretization of the computational domain we employ a fully hexahedral mesh that is refined via a cell-splitting approach in the high-velocity and spray-ignition regions. More specifically, five levels of refinement are used. The smallest cell size is 40 μm and is used in the vicinity of the injection point and the dense-spray region, shown in black color in Figure 1. This size is chosen on the basis of the guidelines of [65] according to which, for a good quality LES of the Spray A configuration, the cell size in the dense-spray region may not exceed 60 μm.

At the next level of refinement, the cell size is 80 μm (grey region); this size is determined on the basis of our earlier simulations [15] of cold spray flow of

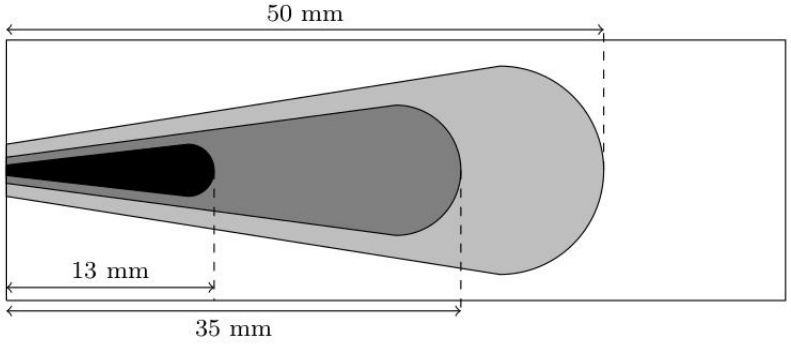


Figure 1: Computational mesh with the various refinement regions. The transition layer consisting of five cells between the white and light grey region is not shown for visibility purposes.

n-dodecane. At the next level, the cell size is set at 160 μm (light gray region in Figure 1). Next we employ a transition layer of five cells whose size 320 μm. Finally, the largest cell size is 640 μm (white region in Figure 1. The extent of the various refinement regions is based on preliminary simulations with n-dodecane and on a reasonable compromise between accuracy and computational cost. The entire computational mesh consists of 11.8 million cells.

In all simulations the time increment has been determined according to the CFL condition with a Courant number equal to 0.3. The end-time of all simulations is set at 1.6 ms.

5. Numerical results

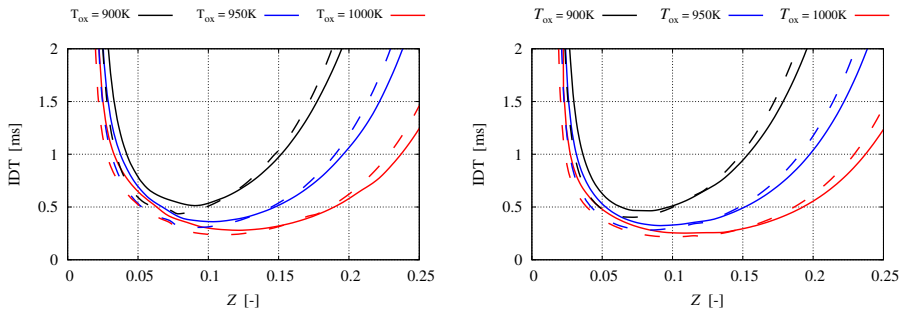
First we present results of the ignition delay time in a homogeneous reactor for both n-dodecane and the KME surrogate. Then we elaborate on the solution of the 1D counterflow diffusion flames and outline the main differences between the cases "15% O_2" and "21% O_2". Next we analyse our numerical predictions for the spray ignition and evolution of the combustion process, while in the fourth and fifth subsections we examine, respectively, the temperature distribution and the mass-fraction distribution of certain species of interest. Comparison between the three cases considered herein are also drawn.

5.1. Ignition delay in a homogeneous reactor

In order to gain some insight on the differences between the ignition of n-dodecane and that of KME surrogate, we provide results for the Ignition Delay Time (IDT) in a 0D homogeneous reactor for each of these two fuels. In our study, for the definition of the IDT, we follow the guideline of ECN [66]. According to it, the Ignition Delay Time (IDT) is defined as the time when the mass fraction of OH reaches 2% of its maximum value. The homogeneous reactor calculations were performed on the basis of the concept of the adiabatic mixing line [67]. The underlying idea of this concept is to consider enthalpy-based inert mixing between fuel and oxidizer. Herein we consider the cases of 15% O_2 and 21% O_2 in the oxidizer. Our calculations were performed with the software *Cantera* [46].

Results for the IDT at different oxidizer temperatures and fuel temperature equal to 363 K are plotted in Figure 2. We observe that in all cases the IDT decreases as the ambient temperature increases. Further, the value of the most reactive mixture fraction Z is on the lean side but it decreases and shifts toward the stoichiometric value as the temperature increases. These observations are consistent with earlier studies of fuel blends containing n-dodecane [20, 68, 69]. It is also interesting to mention that for oxidizer temperature of 900 K, the values of the IDT are higher than those reported in [20] with the n-dodecane mechanism [70]. Also, from the plots of Figure 2, we infer that overall the IDT values for both fuels are very close. Nonetheless, in lean mixtures, the IDT for the KME surrogate is slightly lower than that of pure n-dodecane. Whereas, in rich mixtures the situation is reversed: it is the IDT of n-dodecane that is slightly lower than that of the KME surrogate. Finally, we note that the results for the two oxygen concentrations in the oxidizer, 15% O_2 and 21% O_2 respectively, are very close to one another.

As a sidenote, we may add that, for (pure) n-dodecane and oxidizer temperature of 900 K , the IDT predictions are considerably higher than those of [20] obtained with the mechanism [70]. The difference is due to the fact that the



(a) 15% O_2 **(b)** 21% O_2

Figure 2: Ignition delay time in a 0D homogeneous reactor computed along the adiabatic mixing line at different ambient temperatures and compositions. The solid lines correspond to the KME surrogate and the dashed lines to n-dodecane.

mechanism [54] predicts in general higher IDT values than other mechanisms; this has already been observed in earlier studies [11, 20].

5.2. Flamelet Solution

As mentioned above, the FGM database for each case is constructed on the basis of a canonical configuration, namely the corresponding laminar CD flame. In the CD flame setup, the temperature of the oxidizer and fuel streams are, respectively, the ambient temperature and the initial temperature of the fuel jet inside the combustion chamber of the corresponding physical problem; in this case these correspond to the "Spray A" operating conditions. In other words, the temperature in the oxidizer stream is 900 K and in the fuel stream 363 K. Also, the pressure in the CD flame setup is the same as the ambient pressure of the corresponding physical problem, namely 6 MPa.

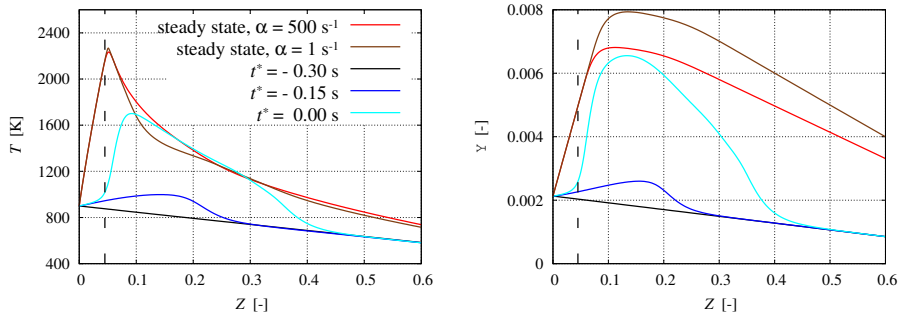
It is noted that, for a given fuel, a generated FGM database corresponds to specific ambient conditions, fuel temperature and oxidizer composition. Accordingly, if any of these quantities is modified, then a separate FGM database has to be constructed. For this reason, the FGM database of the cases "15% O_2" and "15% O_2 hybrid" is different than that of the case"21% O_2".

For the construction of each FGM database we have combined one unsteady solution of the flamelet equations at strain rate $\alpha = 500$ s^{-1} with a large number of steady-state flamelet solutions at strain rates varying between $\alpha = 1$ s^{-1} and 500 s^{-1}.

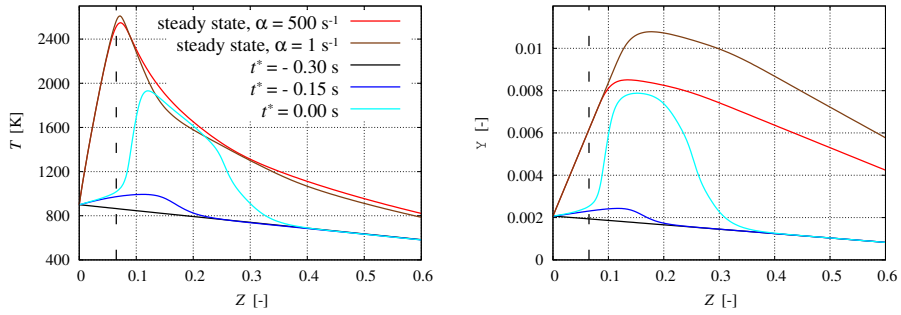
The unsteady solution serves to capture the ignition of the mixture and the transsition to the steady-state solution. In the construction of the database, care has been given to make sure that the transition from the unsteady solution to the steady ones in the $Z - \mathcal{C}$ space is smooth; herein this is achieved via interpolation. Also, in regions where the steady and unsteady solutions overlap, the unsteady solution is selected over the steady one. It is noted that the peak of $\mathcal{Y}$ after ignition slightly exceeds the steady-state value. Beyond this peak, $\mathcal{Y}$ decreases and reaches its steady-state value as the flamelet solution approaches that of chemical equilibrium. Following [17] this part was omitted so as to ensure the monotonicity of the progress variable hence a consistent database.

The IDT in counterflow diffusion flames for oxidizing streams with 15% and 21% O_2 in the oxidizer stream are 0.408 ms and 0.294 ms, respectively. In other words, the difference in the IDT between the two oxidizers is 0.114 ms, which is considerable. We therefore deduce that the ignition starts earlier for the case with higher oxygen concentration, as expected. Further, according to [27], the IDT for the CD flame of pure n-dodecane and 15% O_2 in the oxidizer was predicted to be 0.39 ms with the mechanism of [54]. In other words, the replacement of 35.68% of n-dodecane by methyl butanoate yields only a marginal increase of the IDT.

It is also remarked that the IDT is shorter in spray combustion than in laminar CD flames, mainly due to flow turbulence, which enhances mixing. Figure 3 shows plots of the temperature T and progress variable $\mathcal{Y}$ as functions of Z and at times t^* shifted relative to the IDT, $t^* = t-$IDT, for (a) 15% O_2 and (b) 21% O_2 in the oxidizer stream. From these plots we confirm that by increasing the oxygen concentration in the oxidizer stream, the maximum temperature of the CD flame increases. Also, in both cases, the temperature peak occurs close to the stoichiometric value of Z. With regard to the plots



(a) 15% O_2



(b) 21% O_2

Figure 3: Evolution of the temperature T (left) and progress variable $\mathcal{Y}$ (right) as function of the mixture fraction Z, according to the unsteady flamelet solution (strain rate $\alpha = 500\ \mathrm{s}^{-1}$) at times t^* shifted relative to the corresponding IDT. The vertical dashed line denotes the stoichiometric mixture fraction Z_{st}. (a) 15% O_2 in the oxidizer. (b) 21% O_2 in the oxidizer.

of $\mathcal{Y}$, one can reaffirm the monotonic behaviour of $\mathcal{Y}$ from the mixing line to chemical equilibrium, as well as the convergence of the unsteady solution to the steady one near the stoichiometric value of Z and for high values of $\mathcal{Y}$. Further we observe that, in both cases, $\mathcal{Y}$ peaks in the rich-mixture region.

5.3. Spray ignition and temporal evolution of the flames

When the liquid fuel is initially injected into the combustion chamber, the dominant physical mechanisms are: i) the primary breakup of the liquid jet which leads to the formation of droplets, ii) the subsequent droplet breakup and evaporation, and iii) the mixing of the fuel vapour with the oxidizer. As

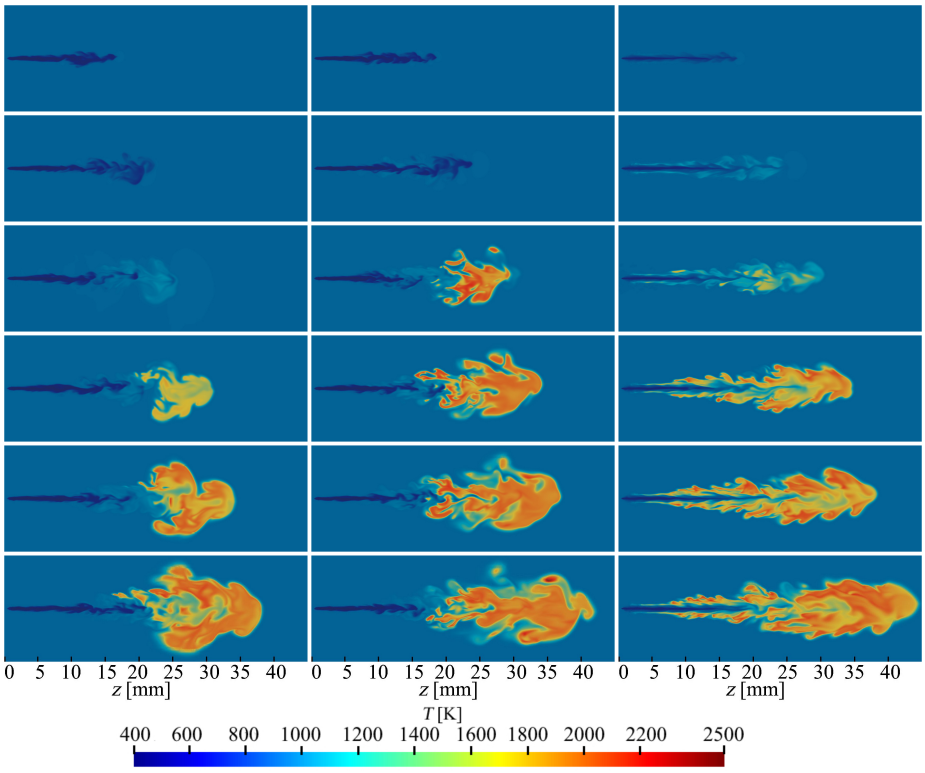


Figure 4: Colour-filled plots of the temperature T at the central vertical plane for the cases "15% O_2" (left), "21% O_2" (centre) and "15% O_2 hybrid" (right), at times $t = 0.1$, 0.2, 0.3, 0.4, 0.5 and 0.65 ms.

mentioned above, we do not directly solve for the primary breakup of the liquid jet, but we account for it by introducing the Rosin-Rammler probability distribution function for the initial diameter of the droplets.

In absence of chemical reactions, the temperature distribution is similar for all three cases considered herein ("15% O_2", "21% O_2" and "15% O_2 hybrid"). This can be inferred from Figure 4 which shows colour-filled plots of the temperature at the central plane and at different time instances for all three cases. In this figure we can observe that the temperature decreases in the region close to the injection position, $z < 10$ mm. This temperature drop is due to interphasial heat exchange and evaporation of the liquid fuel.

As the spray evolves and fuel vapour is getting mixed with the oxidizer, a small amount of heat is released due to combustion in the fuel-rich region of the spray which raises the temperature of the gas by 200 to 300 K. This phenomenon marks the onset of the low-temperature combustion, also known as "first-stage ignition". For the case "15% O_2" this stage starts at $t \approx 0.30$ ms; whereas for the case with higher oxygen concentration, "21% O_2", it starts earlier, $t \approx 0.25$ ms. The same trend, i.e. earlier ignition with increased O_2 concentration, was also observed in the corresponding laminar CD flames. When comparing the cases "15% O_2" and "15% O_2 hybrid", we observe that in the hybrid case the low-temperature combustion starts much earlier, at $t \approx 0.2$ ms, and lasts longer, until $t \approx 0.35$ ms. The longer duration of this stage can be explained by the lower evaporation rate of the fuel in the hybrid case, which is due to the different thermophysical properties of the fuel droplets.

After this stage, the second-stage ignition takes place in the low-velocity region, typically close to the tip and the periphery of the vapour spray. This stage is characterized by the simultaneous formation of multiple self-igniting kernels in these regions. The energy released during this process promotes low-temperature combustion throughout the entire spray. For the cases "15% O_2" and "21% O_2" the second-stage ignition occurs mainly in the tip of the vapour spray. In Figure 4, the temperature distributions at 0.3 ms for the case "15% O_2" and at 0.25 ms for the case "21% O_2" are representative of the second-stage ignition. Concerning the case "15% O_2 hybrid", the second-stage ignition extends on the periphery of the entire vapour spray in the region close to the injection point. The representative temperature distribution of this stage is the one at $t = 0.4$ ms. Therein, we can observe the formation of multiple self-igniting kernels at the periphery of the vapour spray.

After the termination of the second-stage ignition, the high-temperature region expands in all directions while the flame gets stabilized at the Flame Lift-Off Length (FLOL), as it can be inferred from the plots at $t = 0.6$ ms in Figure 4. In other words, at the later stage, the mixture experience a volumetric ignition. This stage is referred to as quasi-stationary state of volumetric expansion of the

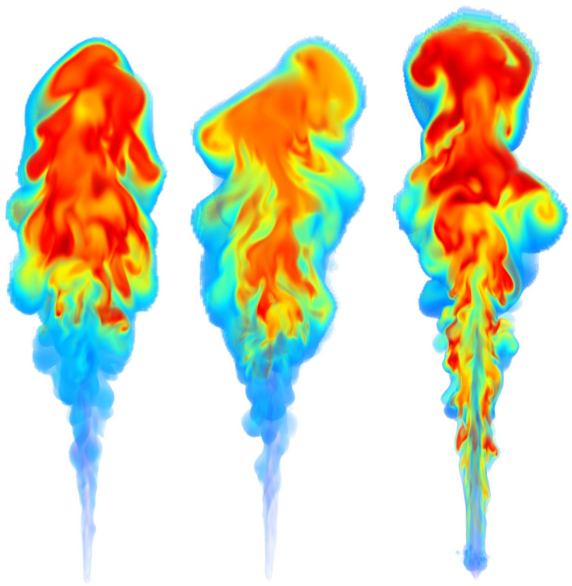


Figure 5: Flame topology at $t = 1$ ms in the cases "15% O_2" (left), "21% O_2" (centre) and "15% O_2 hybrid" (right).

flame. The same sequence of events was also observed in our previous study of n-dodecane spray flames [27], as well as in earlier experimental [71, 72] and numerical [17, 19] studies of spray combustion of pure n-dodecane.

The flame topologies in the cases "15% O_2" and "21% O_2" are quite similar. For visualization purposes, in Figure 5 we present 3D plots of the temperature at $t = 0.1$ ms. Only the cells with $Z > 0.001$ have been taken into account for these colour plots; in other words, we consider only the regions where the fuel is mixed with the oxidizer. Therein we can observe the volumetric expansion of the flame, the regions of the high-temperature and the positions where the flame is stabilized. When comparing the cases "15% O_2" and "21% O_2", we observe that in the region close to the nozzle exit the flame expands in a similar fashion. Also, in the case "21% O_2" the high temperature region extends to regions close to the injection position, which contributes to shorter FLOL.

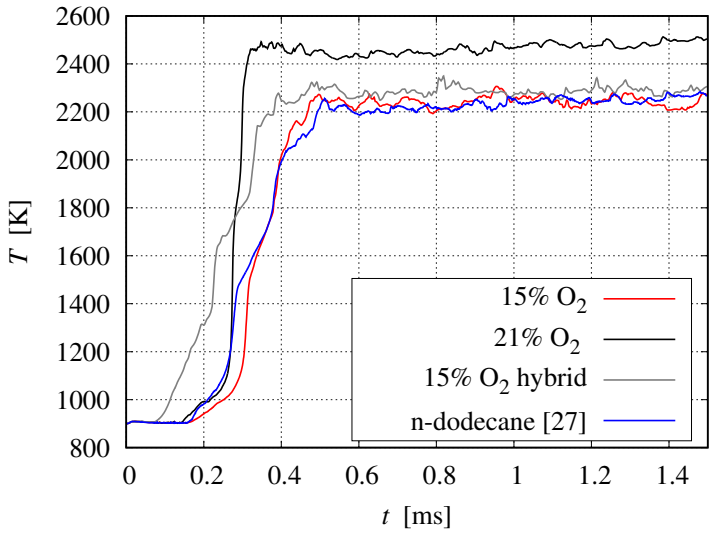


Figure 6: Maximum temperature evolution in the computational domain along with numerical result of [27].

On the contrary, the flame topology in the case "15% O_2 hybrid" and in the region close to the nozzle exit differs substantially from the respective "15% O_2" case. More specifically, the spray develops in the radial direction, normal to the direction of injection of the liquid jet. Presumably, this is due to the higher viscosity of the liquid KME compared to that of the surrogate fuel. This aspect has already been reported in the experimental studies of Corral-Gomez et al. [4] and Bohl et al. [3]. Nonetheless, the radial expansion of the jet after the 1st-stage ignition is slower than in the other cases, which can also be corroborated from the plots of Figure 4.

The aforementioned three ignition stages can be discerned in Figure 6, which depicts the temporal evolution of the maximum temperature in the computational domain. From these plots, we can infer that the mixture ignites earlier for the case "15% O_2 hybrid", while the low-temperature combustion phase is longer compared to the cases "15% O_2" and "21% O_2". Additionally, the initial oxygen concentration has an impact on mixture ignition. More specifically, although the low-temperature combustion starts more or less at the same time

for the cases "15% O_2" and "21% O_2", $t \approx 0.15$ ms, it lasts substantially longer in "15% O_2 (until $t \approx 0.4$ ms vs. $t \approx 0.3$ ms). Also in the case "21% O_2", the mixture ignites and enters the quasi-stationary state of volumetric expansion earlier, at $t \approx 0.25$ ms. Moreover, the time of transition from the first-stage ignition to the quasi-stationary state is much shorter time than in the case "15% O_2".

Our LES predictions for the temperature during the volumetric expansion depend heavily on the oxygen concentration in the oxidizer, as expected. In particular, in the case "21% O_2", the maximum temperature during this stage oscillates around 2500 K, while for both cases with lower oxygen concentration, the maximum temperature is around 2300 K. Overall, the maximum temperature throughout the computational domain is in good agreement with that of the corresponding CD flame, which indicates that turbulence-chemistry interaction is rather weak.

Since the main constituent of the biodiesel is the n-dodecane, it is interesting to compare the present results with our previous simulations of n-dodecane spray flames [27] with the mechanism of [54]. It is noted that in the case "15% O_2" and the simulations [27], the initial composition and thermodynamic state of the ambient gas are the same. Moreover, the combustion mechanism of the biodiesel surrogate incorporates the mechanism [54] for n-dodecane, which further facilitates comparisons. To this end, in Figure 6 we have included the plot of the evolution of the maximum temperature for n-dodecane. We observe that in both cases ("15% O_2" and n-dodecane) the flame develops in the same manner and the ignition process is composed of the three stages described above. Also, the maximum-temperature plots are very close to one another. Our numerical simulations further predicted, for both fuels, the formation of igniting kernels before the volumetric expansion of the flames. Additionally, the location and area of the high-temperature combustion region are similar. These similarities are not surprising since n-dodecane is the main component of the surrogate fuel.

In Figure 7 we provide colour-filled plots of the scaled progress variable $\mathcal{C}$ at different times. We observe that in the very early stage, $t = 0.1$ ms, the

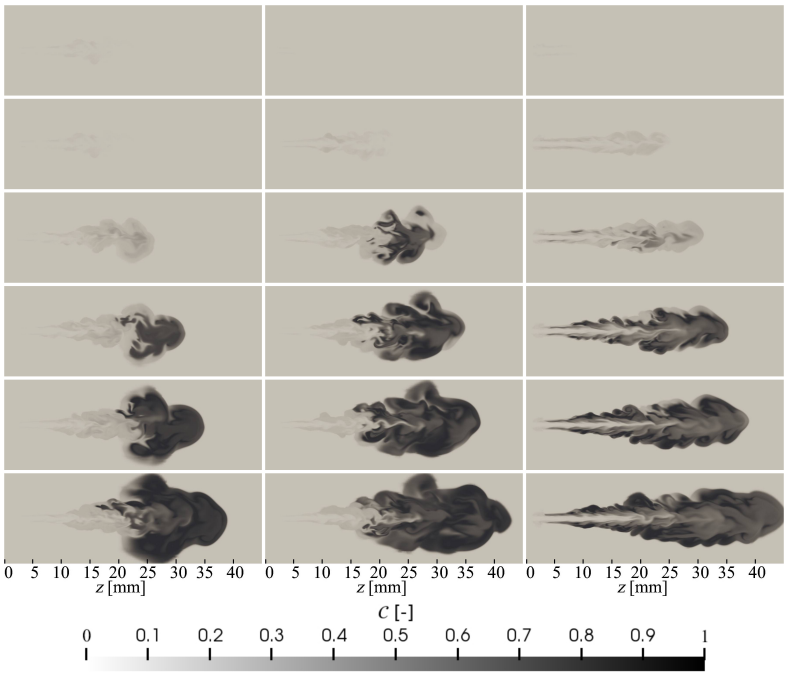


Figure 7: Colour-filled plots of the scaled progress variable, $\mathcal{C}$, at the central vertical plane for the cases "15% O_2" (left), "21% O_2" (centre) and "15% O_2 hybrid" (right), and at times $t = 0.1,\ 0.2,\ 0.3,\ 0.4,\ 0.5$ and 0.65 ms.

main physical phenomena are the droplet breakup and evaporation, without any combustion. The first row of plots in Figure 7 clearly depicts this aspect, wherein the distribution of $\mathcal{C}$ is almost uniform and practically zero throughout the computational domain. As the evaporation process advances, the vapour fuel is mixed with the oxidizer and the gaseous mixture starts to ignite, which is denoted by the increase in the values of $\mathcal{C}$. Overall, the numerical predictions for the cases "15% O_2" and "21% O_2" are quite similar. However, the flame expansion in the axial direction is faster in the case "15% O_2" than in "21% O_2". Additionally, in the case "15% O_2", ignition takes place at a later time and occurs at a larger distance from the injection point, as it can be inferred upon comparison of the plots at $t = 0.4$ ms (for "15% O_2") and $t = 0.3$ ms (for "21% O_2").

On the contrary, our numerical results for the hybrid case, predict higher values of the scaled progress variable in the region close to the nozzle at all times. This implies an earlier onset of the combustion process, leading to earlier ignition and shorter IDT. Moreover, we can identify ignition kernels at the periphery of the spray even at early times.

In the plots of Figure 7, it is also worth noting the volumetric ignition that takes place within multiple ignition kernels at t =0.65 ms for all three cases. Based on these plots, we may deduce that in all three cases the maximum values of $\mathcal{C}$ are attained at the periphery of the spray.

Next, we discuss the predictions of our LES for the IDT and FLOL. For the definition of the FLOL we also follow the guideline of ECN [66]. Thus, the FLOL is defined as the first axial location where the OH mass fraction becomes equal to 2% of its maximum value throughout the domain.

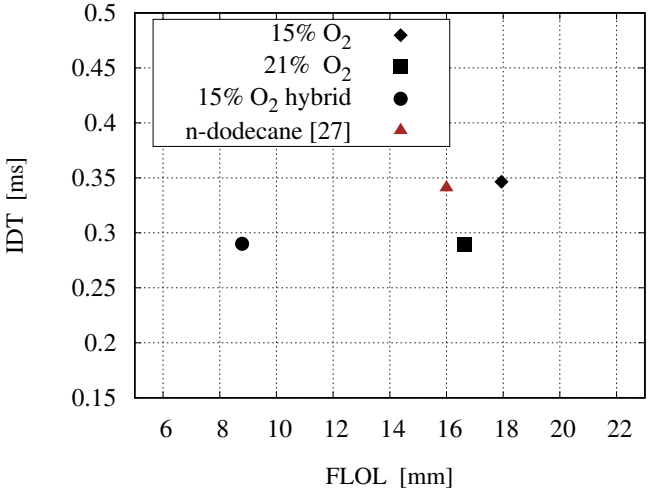


Figure 8: Numerical results for the Ignition delay time (IDT) and flame lift-off length (FLOL).

In Figure 8 we have plotted our numerical predictions for the IDT and FLOL for all three cases considered in our study. We observe that the initial oxygen concentration impacts considerably the IDT and has a smaller effect on the FLOL. More specifically, the IDT decreases from 0.34 ms for "15% O_2" to

0.28 ms for "21% O_2"; in other words, the IDT decreases with the oxygen concentration. The same trend was also observed in the corresponding CD flames that were used to construct the FGM database. With respect to the FLOL, the flame stabilizes at 17.9 mm and 16.6 mm in the cases "15% O_2" and "21% O_2", respectively. Additionally, when comparing the predictions for "15% O_2" with our earlier simulations for n-dodecane, we observe almost no difference in the IDT and a mild difference in the FLOL.

In the hybrid case, the predicted IDT is 0.29 ms, which is considerably shorter than in "15% O_2". More importantly, the flame stabilizes closer to the injection nozzle, at approximately 8.8 mm. In other words, there is a significant decrease in the FLOL in the hybrid case, almost by 50% with respect to the nominal case "15% O_2". In general, a short FLOL does not allow the oxidizer to enter the central part of the spray where combustion occurs mostly at rich conditions. Also, short FLOL does not allow the evaporated fuel to reach areas where combustion takes place under lean conditions. As a result, shorter FLOLs can result in the increase of both soot and NOx emissions [73, 74].

In order to gain some additional physical insight, we examine how the temperature evolves over time in the FLOL region. Figure 9 shows colour-filled plots of T at the radial planes (streamwise stations) $z = 15$ mm and $z = 25$ mm, and at various time instances. According to these plots, the temperature field at $z = 15$ mm, attains low values in the cases "15% O_2" and "21% O_2" but higher values in the hybrid case. The temperature decreases toward the centre of the radial plane, which corresponds to the interior position of the spray. As time advances, the spray at this particular axial location does not expand in the radial direction; instead it remains rather confined within a specific region for all three cases. This is due to the fact that in this region, $z = 15$ mm, the spray is characterized by high axial velocities.

The advancement of the spray downstream is depicted in Figure 9b. As it develops, the velocity drops in its frontal region and mixing intensifies. By comparing the respective plots at $t = 0.3$, 0.4, 0.5 and 1 ms in Figures 9a and 9b, we can discern the expansion of the spray in the radial direction, which is

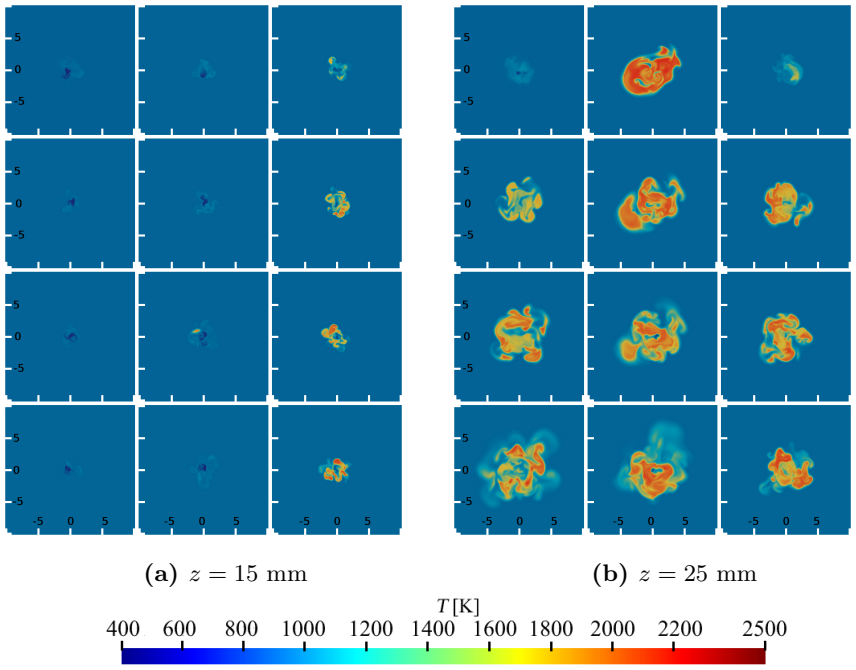


Figure 9: Colour-filled plots of the temperature T at two different radial planes (streamwise stations) for the cases "15% O_2" (left), "21% O_2" (centre) and "15% O_2 hybrid" (right), at times $t = 0.3,\ 0.4,\ 0.5$ and 1 ms. (a) Radial plane $z = 15$ mm. (b) Radial plane $z = 25$ mm.

intensified with the onset of combustion. During this process, strong temperature gradients are developed in the radial direction, which results in increased heat diffusion. At later times, the flame shape and surface area are quite similar for the cases "15% O_2" and "21% O_2"; see, for example the plots at $t = 0.5$ and 1 ms. On the contrary, the flame surface area in the case "15% O_2 hybrid" is considerably smaller. One common feature in all three cases is that the temperature at the centre of the radial planes is always lower than at the periphery. This further corroborates the fact that the combustion takes place in the periphery of the spray, whereas in the centre of the flame there is a cold region comprising of mostly unburned rich mixture.

5.4. Temperature distribution

In this section we elaborate further on the temperature distribution in the spray. For this purpose, the computational domain is divided into four different regions in terms of the axial distance from the nozzle exit: $z < 10$ mm, $10 \leq z < 20$ mm, $20 \leq z < 30$ mm, and $z \geq 30$ mm. Then, the numerical predictions for the temperature are sampled at different time instances in each of these four regions. We note that only sample points above the threshold $Z = 0.001$ have been taken into account in our analysis.

In Figure 10 we present scatter plots of T against Z at different time instances, and for each of the four regions mentioned above. According to them, at $t = 0.1$ ms, liquid fuel evaporation and mixing are dominant close to the injection point. This can be evidenced by the presence of the adiabatic mixture line, along which T decreases as Z increases. The initial oxygen concentration does not impact the temperature distribution at this early stage ($t = 0.1$ ms), as signified by the fact that the scatter plots of the cases "15% O_2" and "21% O_2" are similar. By contrast, for the hybrid case, our numerical results predict higher temperature compared to the "15% O_2" case. Additionally, in the hybrid case, most of the temperature pixels correspond to values of low mixture fraction Z. We can therefore deduce that the evaporation rate in the hybrid case is lower than in the nominal case "15% O_2".

The evolution of the temperature distribution during ignition can be inferred from the plots in Figure 10 as well. When comparing the three cases, the most striking feature at early times is that the temperature distribution begins to scatter much earlier in the cases "15% O_2 hybrid" and "21% O_2". This in turn implies lower IDT. Additionally, on the basis of the temperature peaks at $t = 0.3$ ms, we infer that, in these two cases, ignition takes place in the third region of the domain, $20 \leq z < 30$ mm and at fuel-rich conditions, $Z = 0.17$. Once the mixture has ignited, the temperature increases rapidly, and its peak shifts towards the stoichiometric value. At the same time, the scatter plot of the temperature spreads out.

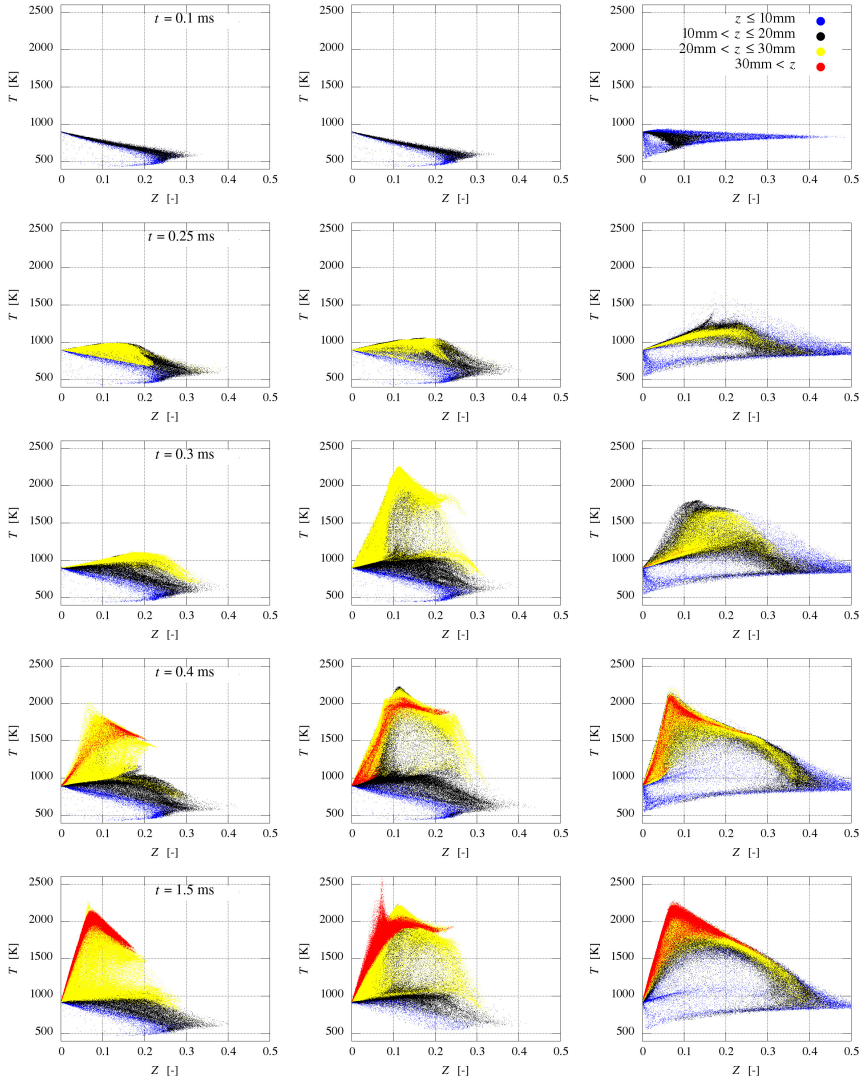


Figure 10: Scatter plot of temperature against mixture fraction, for the cases "15% O_2" (left), "21% O_2" (centre) and "15% O_2 hybrid" (right).

The initial oxygen concentration also has an impact on the overall temperature distribution in the domain. We further observe that for the case "15% O_2" at $t = 1.5$ ms, when the flame has already reached the quasi-stationary state, the temperature in each of the four regions varies within a specific range.

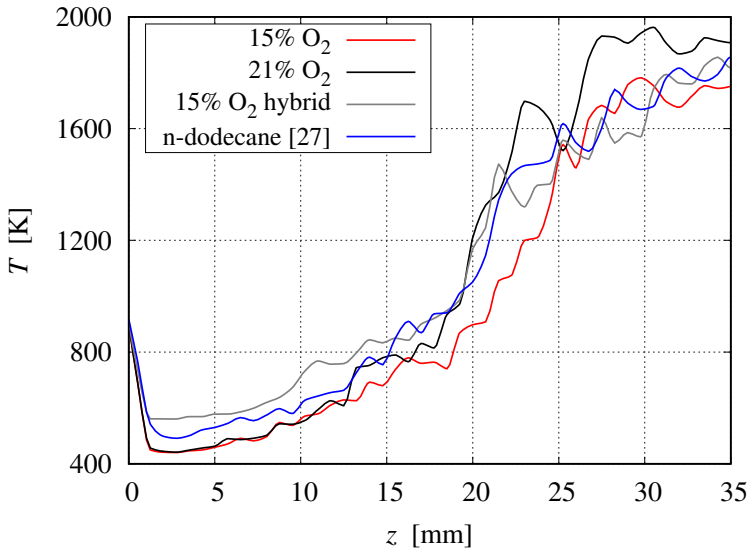


Figure 11: Average temperature along the spray axis between $t = 1$ ms and 1.6 ms.

Moreover, there is very little overlap between the scatter plots in the four regions. Whereas in the "21% O_2" case, the scatter plots in the second region ($10 \leq z < 20$ mm) overlap with the third one ($20 \leq z < 30$ mm), which denotes shorter FLOL compared to that of "15% O_2".

In the hybrid case, the mixture ignites in the second region of the domain, $10 \leq z < 20$ mm, which can be observed from the respective scatter plot at $t = 0.25$ ms. Similarly to the case "15% O_2", the temperature distribution spreads out after the onset of ignition and its peak shifts towards the stoichiometric value. Additionally, for the entire range of Z, most of the sample points correspond to high-temperature values. This feature can be inferred by comparing the "body" of the scatter plots (the area with high concentration of pixels) which shows that it is more populated in the hybrid case than in "15% O_2". Nevertheless, similarly to "15% O_2" case, the temperature peak at later times, $t = 1.5$ ms, is also attained in the fourth region of the domain, $Z > 30$ mm, depicted by the red dots in the plots. Further, the global maximum of the temperature occurs close to the stoichiometric value.

Figure 11 shows plots of time-averaged temperature profiles along the spray axis, with averaging in the interval between $t = 1$ ms and 1.6 ms. According to them, in all three cases the temperature drops rapidly and in a linear fashion away from the injection point. For instance, at $z = 2$ mm, it has already dropped by approximately 450 K in the cases "15% O_2" and "21% O_2", and by 300 K in the hybrid case. The temperature decrease is because of the heat dispensed for the heating and evaporation of the liquid fuel. After attaining its minimum value, the temperature rises. In fact, three different zones of temperature rise can be identified. In the first zone, $2 < z < 18$ mm, the temperature rise occurs at a moderate rate which is the same in all three cases. In the second zone, $18 < z < 27$ mm, the temperature rises at a very high rate, almost by 1000 K in "15% O_2" and by 1200 K in "21% O_2" case. This region indicates the transition from low to high-temperature combustion. In the third zone, $z < 27$ mm, the rate of temperature increase is moderate and similar to that of the first zone.

Comparison of these plots with the equivalent one for n-dodecane, reveals that the initial temperature drop in the case of n-dodecane is 50 K less than in the case "15% O_2". We can therefore presume that the presence of methyl butanoate in the composition of the fuel increases the evaporation rate. This is due to the increase of the surface area of the droplets, which in turn implies that the droplets of the surrogate blend disintegrate faster. Additionally, the enthalpy of evaporation of methyl butanoate is lower than that of n-dodecane, which leads to higher evaporation rates. In the hybrid case the initial temperature drop is smaller, which is attributed to the larger area of ignition kernels and shorter FLOL than in the other two cases.

5.5. Species mass-fraction distributions

In this subsection we examine the mass-fraction distributions of certain important species, namely, formaldehyde CH_2O, hydroxyl OH, hydrogen peroxide H_2O_2 and acetylene C_2H_2. The objective of this analysis is to further assess the influence of the oxygen concentration and liquid-fuel properties on the flame evolution and the combustion process.

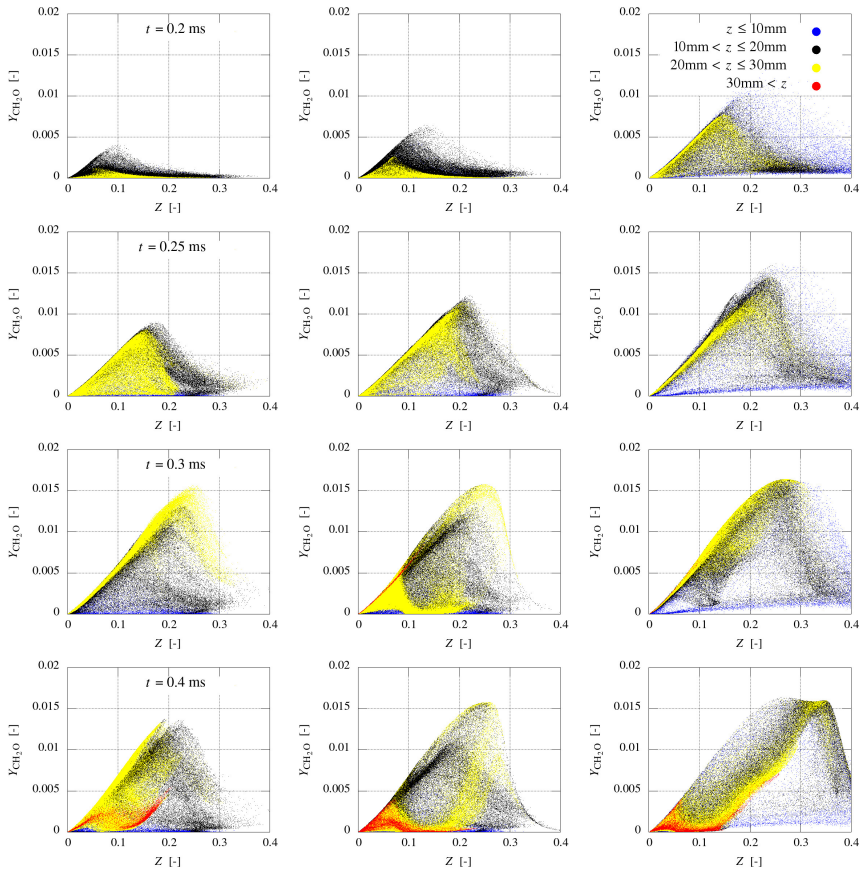


Figure 12: Scatter plot of CH_2O mass fraction against mixture fraction, for the cases "15% O_2" (left), "21% O_2" (centre) and "15% O_2 hybrid" (right).

Actually, CH_2O is the key species that characterizes the transition from low to high-temperature combustion [75], which is also the reason that its concentration enters the definition of the progress variable $\mathcal{Y}$. Also, in our analysis we use CH_2O in order to gauge regions of low-temperature combustion. According to our numerical results, the FLOL is 16 and 18 mm for the cases "15% O_2" and "21% O_2", and 8.8 mm for the hybrid case. Therefore, it is expected that the corresponding regions be characterized by high CH_2O mass fractions concentration. Figure 12 shows scatter plots of the mass fraction of formaldehyde at times $t = 0.2$, 0.25, 0.3 and 0.4 ms. Therein, the computational domain has

been divided into the same four regions as in the scatter plot of the temperature field. According to them, in the cases "15% O_2" and "21% O_2", the CH_2O mass fraction peaks mainly in the region defined by $10 < z \leq 20$ mm and represented by black dots in the plots. As expected, this region encompasses the FLOL. In the case "15% O_2 hybrid", the peak values at early times are attained in the region close to the nozzle $z < 10$ mm (corresponding to blue dots in the plots). As the flame develops, high values of CH_2O are observed in the second region too. The peak value for all three cases stays more or less constant, $Y_{CH_2O} \approx 0.015$, and occurs for $Z = 0.25$. For all cases, the shape of the distribution can be characterized as possessing a negative skewness; however its width in the hybrid cases is larger than in the other two cases.

It is also worth adding that the scatter plot of the CH_2O concentration in "15% O_2" is quite similar to that in the corresponding n-dodecane flame [27]. The only noticeable difference is that the presence of methyl butanoate in "15% O_2" results in mildly higher values of CH_2O concentration in the second and third regions, $10 < z \leq 20$ mm and $30 < z \leq 30$ mm, respectively.

Next, in Figure 13 we present colour-filled plots of the CH_2O mass fraction at the central vertical plane and at different times. In these plots the time instances are shifted relative to the corresponding IDT; accordingly they plots are presented in terms of $t^* = t - \text{IDT}$. The cases "15% O_2" and "21% O_2", share some similarities in the locations and areas where the CH_2O concentration is high. More specifically, high CH_2O concentrations (up to 0.015) are predicted downstream and away from the injection point. Further, in both cases, the regions of flame stabilization and of high-temperature combustion, $z >$ FLOL, are characterized by comparatively low CH_2O concentrations. With regard to the location and area of CH_2O formation, the same trend was predicted in our earlier simulations of n-dodecane spray flames [27]; this is to be expected since n-dodecane is the main ingredient of the surrogate fuel.

For the hybrid case, the most noticeable feature is that CH_2O starts to form early in the region close to the nozzle. Then, for $z < 15$ mm, high CH_2O concentrations are attained at the periphery of the spray. Whereas at larger distances,

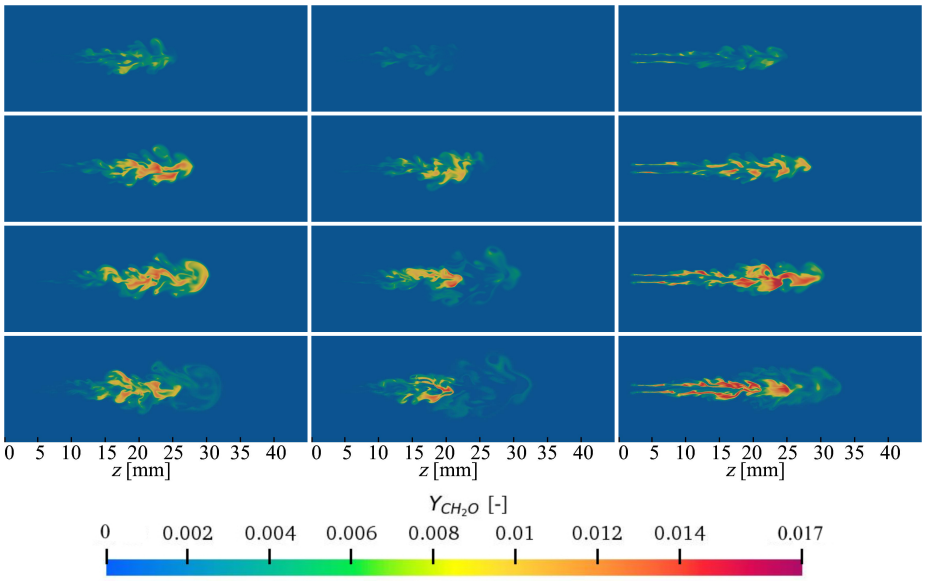
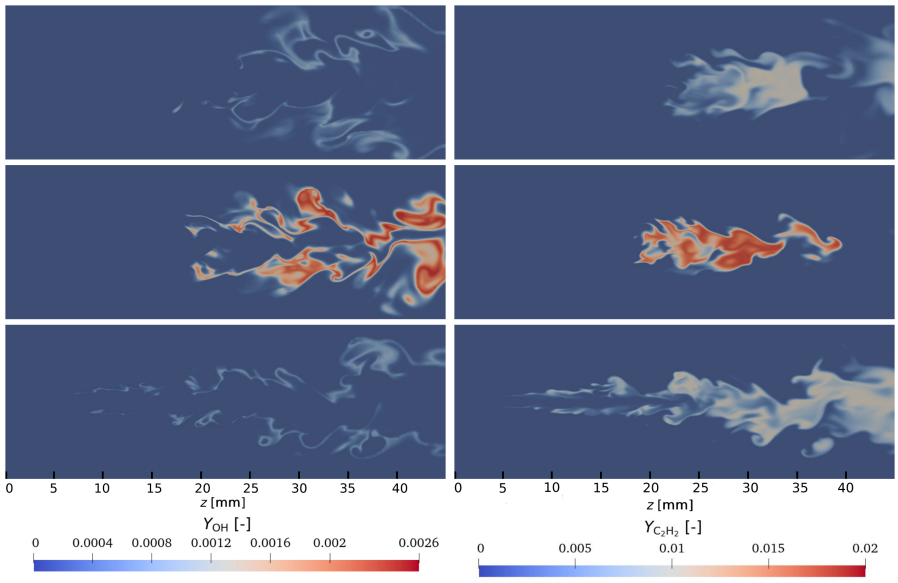


Figure 13: Colour-filled plots of CH_2O mass fraction at the central vertical plane and at times shifted relative to the IDT, $t^* = -0.1,\ -0.05,\ 0,\ 0.05$ ms, for the "15% O_2" (left), "21% O_2" (centre) and "15% O_2 hybrid" (right) cases.

$z > 15$ mm, high values can be found both at the periphery of the spray and close to the spray axis. Therein the CH_2O concentration can be as high as 0.017, i.e. mildly higher than in the other two cases. With regard to the hybrid case, it is also worth noticing in the plots of Figure 13 the formation of several pockets of high CH_2O concentration right before ignition. We can presume that these pockets correspond to the same igniting kernels that were identified in the plots of the temperature field. Finally, comparison of the instantaneous CH_2O mass fractions at $t^* = 0.05$ ms corroborates that the FLOL is much shorter in the hybrid case than in the other two cases; also the FLOL in "21% O_2" is only slightly shorter than in "15% O_2".

Other species whose concentrations are often monitored in both experimental and numerical studies are the hydroxyl radical OH and the acetylene C_2H_2. In fact, areas of high OH concentration correspond to high-temperature combustion. Moreover, C_2H_2 is a soot precursor while OH is a soot oxidizer. It is



(a) OH **(b)** C_2H_2

Figure 14: Colour-filled plots of (a) OH and (b) C_2H_2 mass fractions at the central vertical plane, for the cases "15% O_2" (top), "21% O_2" (middle) and "15% O_2 hybrid" (bottom). The results shown are taken at $t = 1.5$ ms.

therefore interesting to examine the numerical predictions for the distribution of these two species. In Figures 14a and 14b we provide colour-filled plots of the mass fractions of OH and C_2H_2, respectively, at $t = 1.5$ ms.

From Figure 14a we observe that in all cases, the shape and area of the regions of OH formation are similar. However, in "21% O_2" the OH concentration is substantially higher than in "15% O_2" and "15% O_2 hybrid". More specifically, in "21% O_2" the peak value is approximately 0.0026, which is almost 3 times higher than in the other two cases. This difference is to be expected due to the higher availability of oxygen in that case. Further, the peak values in the hybrid case are close to those in "15% O_2"; this is not surprising because the difference between "15% O_2" and "15% O_2 hybrid" is in the liquid fuel properties whereas OH concentration relates to high-temperature (gaseous) combustion. Moreover, in "15% O_2", both the peak value and the region with

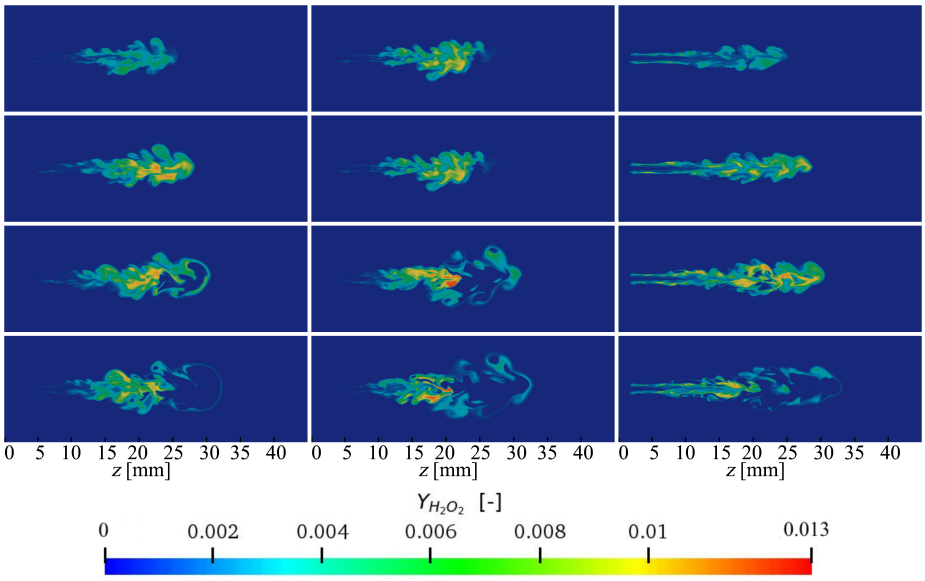


Figure 15: colour-filled plots of H_2O_2 mass fraction at the central vertical plane and at times shifted relative to the IDT, $t^* = -0.1,\ -0.05,\ 0,\ 0.05$ ms, for the "15% O_2" (left), "21% O_2" (centre) and "15% O_2 hybrid" (right) cases.

high OH concentration are similar to those in the corresponding spray flame of pure n-dodecane [27]; once again, this is attributed to the fact that n-dodecane is the main component of the surrogate fuel.

The same trends are predicted for the C_2H_2 concentration. In other words, by increasing the initial amount of oxygen from 15% to 21%, the C_2H_2 concentration increases by a factor of 3. In the plots of Figure 14b, it is interesting to observe that the areas of high C_2H_2 concentration are bordered by areas of high OH mass fractions. Moreover, in the hybrid case we observe significant concentration of C_2H_2 close to the nozzle exit, i.e. in areas of low OH concentration. Since OH is a main oxidizer for soot particles, the soot formed close to the nozzle exit will most likely not be oxidized. This suggests that the hybrid case may result in higher soot concentration in the combustion products.

Finally, we present numerical results for the formation and consumption of hydrogen peroxide, H_2O_2. This species is gauged due to its interesting combus-

tion properties; for example, it can be used as a bipropellant when combined with other fuels since [76, 77]. Figure 15 shows plots of the mass fraction of H_2O_2 at the central vertical plane and at different times relative to the corresponding IDT, $t^* = t - \mathrm{IDT} = -0.1$, -0.05, 0 and 0.05 ms. As in the case of spray combustion of n-dodecane [27], we can identify two stages of H_2O_2 formation and consumption. In the first stage, H_2O_2 is formed before the onset of the (low-temperature) first-stage ignition and throughout the spray region. This stage is well depicted in the plots at $t^* = -0.1$ and -0.05 ms, for the cases "15% O_2" and "21% O_2" respectively. Whereas in the case "15% O_2 hybrid", this stage is prolonged until $t^* = 0$ ms. Also, formation of hydrogen peroxide starts earlier in "15% O_2" than in "21% O_2".

The second stage takes place after ignition and is characterised by consumption of H_2O_2 at high-temperature regions and formation at low-temperature ones. Additionally, we observe that, in the hybrid case, formation of H_2O_2 occurs closer to the injection point than in the other two cases. Further, in the hybrid case there are areas of high H_2O_2 concentrations at longer distances, but once H_2O_2 is consumed, the area of significant concentration extends only up to $z = 20 - 25$ mm, which is the same as in the other two cases. Globally, our simulations indicate that the initial oxygen concentration does not play a major role in the concentration of this species, while the liquid fuel properties have an effect on the location and the area where H_2O_2 is formed.

6. Conclusion

In this study, we have presented LES results for three different types of spray flames with biodiesel surrogates. The initial conditions follow closely the reactive Spray A [66] operating conditions. In our study, the LES approach is coupled with the implementation of the FGM methodology introduced in [27]. According to it, the energy equation is cast in terms of sensible enthalpy, while the heat due to the combustion is calculated from the FGM database through the control variables. The properties of the mixture are approximated

on the basis of six major species, namely, n-dodecane $C_{12}H_{26}$, methyl butanoate $C_5H_{10}O_2$, O_2, CO_2, H_2O and N_2. The advancement of the combustion model is taken into account via the chemical kinetics model of KME surrogate, consisting of oxidation reactions for n-dodecane and methyl butanoate. Furthermore, the secondary breakup of the droplets was modelled via the Modified Taylor Analogy Breakup model [15].

In all three cases we employed the gaseous fuel properties of the biodiesel surrogate. Also, in the cases "15% O_2" and "21% O_2" we used the liquid fuel properties of the surrogate but considered different initial amounts of oxygen. Whereas in the case "15% O_2 hybrid" we employed the liquid fuel properties of the KME itself and the gaseous fuel properties of the surrogate. This setup allows to assess how the initial oxygen concentration and liquid fuel properties impact the various stages of the combustion process.

Our simulations predicted that in all cases the ignition process consists of the same three stages (first and second stage ignition, and volumetric flame expansion) as those observed in n-dodecane flames. However, increased oxygen concentration accelerates ignition and leads to higher combustion temperatures and has a mild influence on the FLOL. Nonetheless, it does not significantly modify the global characteristics and topology of the flame.

On the other hand, the liquid fuel properties have a significant impact on the main characteristics of the combustion process and the flame topology. In particular, employing the liquid KME properties, instead of those of the surrogate, leads to a much shorter FLOL (decrease by a factor of 2) and also shorter IDT. Nonetheless, even though in the hybrid case the mixture starts to react earlier, the advancement of the low-temperature combustion (before the first-stage ignition) is slower than in the other cases. Moreover, whereas in the cases "15% O_2" and "21% O_2", the second-stage ignition occurs mainly in the frontal area of the spray, in the hybrid case it extends on the periphery of the entire vapour spray in the region close to the injection point. These features have an effect on the concentration of certain important species, such as OH, H_2O_2, CH_2O and C_2H_2. In particular, our simulations predicted high concentration of acetylene

(a soot precursor) in areas of relatively low temperature and low concentration of OH (a soot oxidizer), such as close to the nozzle exit. This, in turn, may have an impact on the rate of soot formation.

Acknowledgments. The authors extend their thanks to Dr. K. Moshammer for supplying experimental data of the liquid fuel properties of KME and to Dr. A. Lele for providing the chemical kinetics mechanism of the biodiesel surrogate. The financial support of the National Research Fund of Belgium (FNRS) in the form of the ERANET BiofCFD project is also gratefully acknowledged.

References

[1] K. Anand, R. Sharma, P. Mehta, Experimental investigations on combustion of jatropha methyl ester in a turbocharged direct-injection diesel engine, Proceedings of the Institution of Mechanical Engineers, Part D: Journal of Automobile Engineering 222 (2008) 1865–1877.

[2] H. Ng, S. Gan, Combustion performance and exhaust emissions from the non-pressurised combustion of palm oil biodiesel blends, Applied Thermal Engineering 30 (2010) 2476–2484.

[3] T. Bohl, G. Tian, A. Smallbone, A. Roskilly, Macroscopic spray characteristics of next-generation bio-derived diesel fuels in comparison to mineral diesel, Applied Energy 186 (2017) 562–573.

[4] L. Corral-Gòmez, G. Rubio-Gòmez, S. Martìnez-Martìnez, F. Sànchez-Cruz, Effect of diesel-biodiesel-ethanol blends on the spray macroscopic parameters in a common-rail diesel injection system, Fuel 241 (2019) 876–883.

[5] D. Han, J. Zhai, Y. Duan, D. Ju, H. Lin, Z. Huang, Macroscopic and microscopic spray characteristics of fatty acid esters on a common rail injection system, Fuel 203 (2017) 370–379.

[6] B. Poling, J. Prausnitz, J. O'Connell, The Properties of Gases and Liquids, Chemical Engineering Series, Mcgraw-hill, 2000.

[7] K. Anand, R. Sharma, P. Mehta, A comprehensive approach for estimating thermo-physical properties of biodiesel fuels, Applied Thermal Engineering 31 (2011) 235–242.

[8] B. Sajjadi, A. A. A. Raman, H. Arandiyan, A comprehensive review on properties of edible and non-edible vegetable oil-based biodiesel: Composition, specifications and prediction models, Renewable and Sustainable Energy Reviews 63 (2016) 62–92.

[9] K. R. Bukkarapu, A. Krishnasamy, A critical review on available models to predict engine fuel properties of biodiesel, Renewable and Sustainable Energy Reviews 155 (2022) 111925.

[10] W. A. Sirignano, Fluid Dynamics and Transport of Droplets and Sprays, 2nd Edition, Cambridge University Press, 2010.

[11] A. Wehrfritz, V. Vuorinen, O. Kaario, M. Larmi, Large Eddy Simulation of high-velocity fuel sprays: Studying mesh resolution and breakup model effects for Spray A, Atomization and Sprays 23 (2013) 419–442.

[12] T. Lucchini, G. D'Errico, G. Hardy, N. Maes, N. Dam, B. Somers, Experimental and numerical analyses of liquid and spray penetration under heavy-duty diesel engine conditions, SAE International Journal of Fuels and Lubricants 9 (2016) 108–124.

[13] H. Grosshans, M. Griesing, M. Mnckedieck, T. Hellwig, B. Walther, S. R. Gopireddy, R. Sedelmayer, W. Pauer, H. U. Moritz, N. A. Urbanetz, E. Gutheil, Numerical and experimental study of the drying of bicomponent droplets under various drying conditions, International Journal of Heat and Mass Transfer 96 (2016) 97–109.

[14] J. Solsvik, V. T. Skjervold, L. Han, H. Luo, H. A. Jakobsen, A theoretical study on drop breakup modeling in turbulent flows: The inertial subrange

versus the entire spectrum of isotropic turbulence, Chemical Engineering Science 149 (2016) 249–265.

[15] C. Sula, H. Grosshans, M. Papalexandris, Assessment of droplet breakup models for spray flow simulations, Flow, Turbulence and Combustion 105 (2020) 889–914.

[16] T. Lucchini, G. DErrico, D. Ettorre, G. Ferrari, Numerical investigation of non-reacting and reacting diesel sprays in constant-volume vessels, SAE International Journal of Fuels and Lubricants 2 (2009) 966–975.

[17] A. Wehrfritz, O. Kaario, V. Vuorinen, B. Somers, Large Eddy Simulation of n-dodecane spray flames using Flamelet Generated Manifolds, Combustion and Flame 167 (2016) 113–131.

[18] L. Ma, D. Roekaerts, Modeling of spray jet flame under MILD condition with non-adiabatic FGM and a new conditional droplet injection model, Combustion and Flame 165 (2016) 402–423.

[19] H. Kahila, A. Wehrfritz, O. Kaario, M. Ghaderi Masouleh, N. Maes, B. Somers, V. Vuorinen, Large-eddy simulation on the influence of injection pressure in reacting Spray A, Combustion and Flame 191 (2018) 142–159.

[20] B. Tekgül, H. Kahila, O. Kaario, V. Vuorinen, Large-eddy simulation of dual-fuel spray ignition at different ambient temperatures, Combustion and Flame 215 (2020) 51–65.

[21] F. Jurić, M. Stipiś, N. Samec, M. Hriberşek, S. Honus, M. Vujanović, Numerical investigation of multiphase reactive processes using flamelet generated manifold approach and extended coherent flame combustion model, Energy Conversion and Management 240 (2021) 114261.

[22] A. Demirbas, Progress and recent trends in biodiesel fuels, Energy Conversion and Management 50 (2009) 14–34.

[23] C. Westbrook, C. Naik, O. Herbinet, W. Pitz, M. Mehl, S. Sarathy, H. Curran, Detailed chemical kinetic reaction mechanisms for soy and rapeseed biodiesel fuels, Combustion and Flame 158 (2011) 742–755.

[24] J. Brakora, Y. Ra, R. Reitz, J. McFarlane, C. Daw, Development and validation of a reduced reaction mechanism for biodiesel-fueled engine simulations, SAE International Journal of Fuels and Lubricants 1 (2008) 675–702.

[25] H. An, W. Yang, A. Maghbouli, J. Li, K. Chua, A skeletal mechanism for biodiesel blend surrogates combustion, Energy Conversion and Management 81 (2014) 51–59.

[26] T. Lucchini, D. Pontoni, G. DErrico, B. Somers, Modeling diesel combustion with tabulated kinetics and different flame structure assumptions based on flamelet approach, International Journal of Engine Research 21 (2020) 89–100.

[27] C. Sula, H. Grosshans, M. Papalexandris, Large-eddy simulations of Spray A flames using explicit coupling of the energy equation with the FGM database, Flow, Turbulence and Combustion 109 (2022) 193–223.

[28] A. Lele, S. Vallabhuni, K. Moshammer, R. Fernandes, A. Krishnasamy, K. Narayanaswamy, Experimental and chemical kinetic modeling investigation of methyl butanoate as a component of biodiesel surrogate, Combustion and Flame 197 (2018) 49–64.

[29] K. Anand, Y. Ra, R. Reitz, B. Bunting, Surrogate model development for fuels for advanced combustion engines, Energy & Fuels 25.

[30] K. Moshammer, Temperature-dependend density and viscosity measurements of indian origin biodiesel (unpublished data).

[31] A. Favre, Turbulence - space-time statistical properties and behavior in supersonic flows, Physics of Fluids 26 (1983) 2851–2863.

[32] T. Poinsot, D. Veynante, Theoretical and Numerical Combustion, 2nd Edition, R.T. Edwards Inc., Philadelphia, PA, 2005.

[33] M. Papalexandris, Combustion and Fuels, Presses Universitaires Louvain, Belgium, 2020.

[34] R. Bilger, S. Strner, R. Kee, On reduced mechanisms for methane-air combustion in nonpremixed flames, Combustion and Flame 80 (1990) 135–149.

[35] J. C. Sutherland, P. J. Smith, J. H. Chen, Quantification of differential diffusion in nonpremixed systems, Combustion Theory and Modelling 9 (2005) 365–383.

[36] A. Maghbouli, B. Akkurt, T. Lucchini, G. D'Errico, N. G. Deen, B. Somers, Modelling compression ignition engines by incorporation of the flamelet generated manifolds combustion closure, Combustion Theory and Modelling 23 (2019) 414–438.

[37] A. Hadadpour, S.Xu, K. Pang, X. Bai, M. Jangi, Effects of pre-injection on ignition, combustion and emissions of spray under engine-like conditions, Combustion and Flame 241 (2022) 112082.

[38] C. D. Pierce, P. Moin, A dynamic model for subgrid-scale variance and dissipation rate of a conserved scalar, Physics of Fluids 10 (1998) 3041–3044.

[39] G. Balarac, H. Pitsch, V. Raman, Development of a dynamic model for the subfilter scalar variance using the concept of optimal estimators, Physics of Fluids 20 (2008) 035114.

[40] C. Wilke, A viscosity equation for gas mixtures, Journal of Chemical Physics 18 (1950) 517–519.

[41] A. Burcat, B. Ruscic, Third millenium ideal gas and condensed phase thermochemical database for combustion (with update from active thermochemical tables)., Argonne National Laboratory Technical Report ANL-05/20 and Technion – Israel Inst. of Tech. Report TAE 960.

[42] A. Yoshizawa, Statistical theory for compressible turbulent shear flows, with the application to subgrid modeling, Physics of Fluids 29 (1987) 2152–2164.

[43] X. Chai, K. Mahesh, Dynamic k-equation model for large-eddy simulation of compressible flows, Journal of Fluid Mechanics 699 (2012) 385–413.

[44] L. Vervisch, R. Hauguel, P. Domingo, M. Rullaud, Three facets of turbulent combustion modelling: DNS of premixed V-flame, LES of lifted nonpremixed flame and RANS of jet-flame, Journal of Turbulence 5 (2004) N4.

[45] A. Long, R. Speth, W. Green, Ember: An open-source, transient solver for 1D reacting flow using large kinetic models, applied to strained extinction, Combustion and Flame 195 (2018) 1–12.

[46] D. G. Goodwin, R. L. Speth, H. K. Moffat, B. W. Weber, Cantera: an object-oriented software toolkit for chemical kinetics, thermodynamics, and transport processes, `https://www.cantera.org`, version 2.5.1 (2021).

[47] R. Issa, Solution of the implicitly discretised fluid flow equations by operator-splitting, Journal of Computational Physics 62 (1986) 40–65.

[48] J. Dukowicz, A particle-fluid numerical model for liquid sprays, Journal of Computational Physics 35 (1980) 229–252.

[49] A. A. Amsden, P. J. O'Rourke, T. D. Butler, KIVA-II: A computer program for chemically reactive flows with sprays, Los Alamos National Lab. REP. LA-11560-MS DE89012805.

[50] W. E. Ranz, W. R. Marshall, Evaporation from drops: Part I, Chemical Engineering Progress 48 (3) (1952) 141–146.

[51] W. E. Ranz, W. R. Marshall, Evaporation from drops: Part II, Chemical Engineering Progress 48 (3) (1952) 173–180.

[52] P. J. O'Rourke, A. A. Amsden, The TAB method for numerical calculation of spray droplet breakup, in: SAE Technical Paper Series, 872089, SAE International, 1987.

[53] J. Yu, Y. Ju, X. Gou, Surrogate fuel formulation for oxygenated and hydrocarbon fuels by using the molecular structures and functional groups, Fuel 166 (2016) 211–218.

[54] K. Narayanaswamy, P. Pepiot, H. Pitsch, A chemical mechanism for low to high temperature oxidation of n-dodecane as a component of transportation fuel surrogates, Combustion and Flame 161 (2014) 866–884.

[55] S. Dooley, H. Curran, J. Simmie, Autoignition measurements and a validated kinetic model for the biodiesel surrogate, methyl butanoate, Combustion and Flame 153 (2008) 2–32.

[56] P. Pepiot-Desjardins, H. Pitsch, An efficient error-propagation-based reduction method for large chemical kinetic mechanisms, Combustion and Flame 154 (2008) 67–81.

[57] S. Sahasrabudhe, V. Rodriguez-Martinez, M. O'Meara, B. Farkas, Density, viscosity, and surface tension of five vegetable oils at elevated temperatures: Measurement and modeling, International Journal of Food Properties 20 (2017) 1965–1981.

[58] S. Mishra, A. Krishnasamy, A composition based approach for predicting performance and emission characteristics of biodiesel fuelled engine, in: International Powertrains, Fuels & Lubricants Meeting, SAE International, 2017.

[59] B. Mathew, J. Thangaraja, A. Sivaramakrishna, Combustion, performance and emission characteristics of blends of methyl esters and modified methyl esters of karanja and waste cooking oil on a turbocharged CRDI engine, Clean Technologies and Environmental Policy 21 (2019) 1791–1807.

[60] L. Constantinou, R. Gani, New group contribution method for estimating properties of pure compounds, AIChE Journal 40 (1994) 1697–1710.

[61] L. Constantinou, R. Gani, J. O'Connell, Estimation of the acentric factor and the liquid molar volume at 298 k using a new group contribution method, Fluid Phase Equilibria 103 (1995) 11–22.

[62] K. G. Joback, A unified approach to physical property estimation using multivariate statistical techniques, Ph.D. thesis, Massachusetts Institute of Technology (1984).

[63] W. Kay, Gases and vapors at high temperature and pressure - density of dydrocarbon, Industrial & Engineering Chemistry 28 (1936) 1014–1019.

[64] J. Prausnitz, R. Gunn, Pseudocritical constants from volumetric data for gas mixtures, AIChE Journal 4(4) (1958) 494–494.

[65] Q. Xue, S. Som, P. K. Senecal, E. Pomraning, Large eddy simulation of fuel-spray under non-reacting IC engine conditions, Atomization and Sprays 23 (2013) 925–955.

[66] Engine Combustion Network, Spray A operating condition, `https://ecn.sandia.gov/diesel-spray-combustion/target-condition/spray-ab/` (2021).

[67] E. Mastorakos, Ignition of turbulent non-premixed flames, Progress in Energy and Combustion Science 35 (2009) 57–97.

[68] J. Kannan, M. Gadalla, B. Tekgul, S. Karimkashi, O. Kaario, V. Vuorinen, Large eddy simulation of diesel sprayassisted dual-fuel ignition: A comparative study on two n-dodecane mechanisms at different ambient temperatures, International Journal of Engine Research 22 (2020) 2521–2532.

[69] J. Kannan, M. Gadalla, B. Tekgul, S. Karimkashi, O. Kaario, V. Vuorinen, Large-eddy simulation of tri-fuel ignition: diesel spray-assisted ignition of

lean hydrogenmethaneair mixtures, Combustion Theory and Modelling 25 (2020) 436–459.

[70] T. Yao, Y. Pei, B. Zhong, S. Som, T. Lu, K. Luo, A compact skeletal mechanism for n-dodecane with optimized semi-global low-temperature chemistry for diesel engine simulations, Fuel 191 (2017) 339–349.

[71] E. Oldenhof, M. Tummers, E. Veen, D. Roekaerts, Ignition kernel formation and lift-off behaviour of jet-in-hot-coflow flames, Combustion and Flame 157 (2010) 1553–1563.

[72] S. Skeen, J. Manin, L. Pickett, Simultaneous formaldehyde PLIF and high-speed schlieren imaging for ignition visualization in high-pressure spray flames, Proceedings of the Combustion Institute 35 (2015) 3167–3174.

[73] J. Chomiak, A. Karlsson, Flame liftoff in diesel sprays, Symposium (International) on Combustion 26 (1996) 2557–2564.

[74] D. Siebers, B. Higgins, Flame lift-off on direct-injection diesel sprays under quiescent conditions, in: SAE 2001 World Congress, SAE International, 2001.

[75] R. Klein, L. Schoen, Role of Formaldehyde in Combustion, American Chemical Society, Washington, D.C., 1958, Ch. 6, pp. 58–68.

[76] S. Li, X. Wei, Ignition delay characteristics of kerosene with decomposed hydrogen peroxide, Journal of Propulsion and Power 32 (2016) 431–438.

[77] B. Gribi, Y. Lin, X. Hui, C. Zhang, C.-J. Sung, Effects of hydrogen peroxide addition on combustion characteristics of n-decane/air mixtures, Fuel 223 (2018) 324–333.